

# Quasinormal modes and their excitation beyond general relativity. II: isospectrality loss in gravitational waveforms

Hector O. Silva,<sup>1,2</sup> Giovanni Tambalo,<sup>3</sup> Kostas Glampedakis,<sup>4,5</sup> and Kent Yagi<sup>6</sup>

<sup>1</sup>*Department of Physics and Illinois Center for Advanced Studies of the Universe, The Grainger College of Engineering, University of Illinois Urbana-Champaign, Urbana, Illinois 61801, USA*

<sup>2</sup>*Max Planck Institute for Gravitational Physics (Albert Einstein Institute), D-14476 Potsdam, Germany*

<sup>3</sup>*Institut für Theoretische Physik, ETH Zürich, 8093 Zürich, Switzerland*

<sup>4</sup>*Departamento de Física, Universidad de Murcia, Murcia, E-30100, Spain*

<sup>5</sup>*Theoretical Astrophysics, University of Tübingen, Auf der Morgenstelle 10, D-72076 Tübingen, Germany*

<sup>6</sup>*Department of Physics, University of Virginia, Charlottesville, Virginia 22904, USA*

We continue our series of papers where we study the quasinormal modes, and their excitation, of black holes in the simplest beyond general relativity model in which first-principle calculations are tractable: a nonrotating black hole in an effective-field-theory extension of general relativity with cubic-in-curvature terms. In this theory, the equivalence between the quasinormal mode spectra associated with metric perturbations of polar and axial parities (“isospectrality”) of the Schwarzschild black hole in general relativity no longer holds. How does this loss of isospectrality translate into the time-domain ringdown of gravitational waves? Given such a ringdown, can we identify the two “fundamental quasinormal modes” associated to the two metric-perturbation parities? We study these questions through a large suite of time-domain numerical simulations, by a prescription on how to relate the gauge-invariant master functions that describe metric perturbations of each parity with the gravitational polarizations. Under the assumptions made in our calculations, we find that it is in general difficult to identify either of the two fundamental modes from the time series, although finding evidence for a non-general-relativistic mode is possible sometimes. We discuss our results in light of our assumptions and speculate about what may occur when they are relaxed.

## CONTENTS

I. Introduction	2	B. The wave equation with a position-dependent propagation speed	18
II. Action and field equations	2	1. Change of variable to $c_s = 1$	18
III. Black hole perturbations	3	2. The metric-perturbation case	18
A. Review of the main equations	3	3. Numerical simulations	19
B. First-order form of the wave equation and initial data	4	C. Dependence of the quasinormal frequency extraction on the initial data	20
IV. Numerical results	5	References	21
A. General relativity	5		
B. Beyond general relativity	6		
1. Effects of the variable propagation speed	6		
2. Waveform comparison	7		
3. Spectral content of the waveforms	8		
V. Observational implications	10		
A. Gravitational wave polarizations	11		
B. Synthetic signal generation: a toy model	11		
C. Quasinormal frequency extraction	12		
1. Theory-agnostic single-frequency fits	12		
2. Can we infer a nonzero $\varepsilon$ ?	13		
VI. Conclusions and outlook	15		
Acknowledgements	15		
A. Code details and validation	16		
1. Grid size and boundary conditions	16		
2. Initial data and waveform extraction	16		
3. Convergence tests and error estimates	17		

## I. INTRODUCTION

The response of black holes to linear perturbations is known to be partially described by a superposition of quasinormal modes, associated with complex-valued frequencies [1–3]. The real and imaginary parts of these quasinormal frequencies dictate the oscillation frequency and damping time of each mode, respectively. The hole’s response thus exhibits a characteristic ringdown.

In general relativity, the end state of the ringdown is a Kerr black hole, whose mass  $M$  and spin  $a$  completely determine its quasinormal-mode spectrum [4]. This suggests the idea that the identification of two or more quasinormal frequencies from gravitational-wave data may be used to infer the remnant’s mass and spin. In analogy to using spectral lines to identify atomic and chemical elements, this idea is called black hole spectroscopy [5]; see Ref. [6] for a review. The materialization of this “black hole spectroscopy” program is a key scientific goal of current and future gravitational wave observatories.

Can black hole spectroscopy be used to test fundamental aspects of general relativity? A notable property of the quasinormal mode spectrum of the static limit of the Kerr solution is that the spectrum associated to the two ways metric perturbations can transform under parity transformation [7–9], often called “axial” and “polar,” are the same [10–12]; see also Ref. [13]. The spectra are said to be isospectral. In vacuum general relativity, this property persists beyond the Schwarzschild solution, holding perturbatively in a small-spin expansion [14].

Isospectrality is, however, fragile and known to break in most extensions to Einstein’s theory; see Ref [6], Sec. 3. This is akin to the splitting of degenerate spectral lines by an external electromagnetic field; see Fig. 1. (Theories that preserve isospectrality in some cases are also known [15, 16].)

In our previous work [17], we initiated a program to understand *ab initio* the quasinormal modes and their excitation in the simplest well-motivated beyond general relativity model in which first-principle calculations are tractable: a nonrotating black hole in an effective-field-theory (EFT) extension of general relativity with cubic-curvature terms. Among other results, we reported the first calculation of quasinormal-mode excitation factors beyond general relativity and began exploring the implications of isospectrality breaking in the ringdown of black holes in this EFT.

The purpose of this paper is to continue that work. In particular, we turn from frequency-domain to time-domain calculations. We study the linear response of black holes in the EFT to external perturbations, and suggest how we can use these results to obtain the gravitational-wave polarizations. These results will be used to investigate the impact of the presence of a doublet of fundamental quasinormal mode frequencies in the ringdown, and to what extent we can infer their presence in the waveform.

This work is organized as follows. In Sec. II, we review the EFT of general relativity, as well as the background

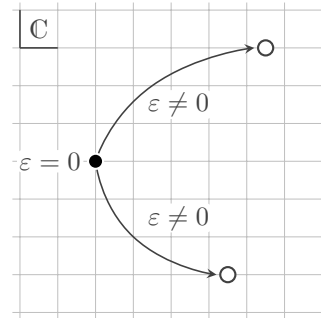


FIG. 1. Illustration of isospectrality breaking. Two degenerate quasinormal frequencies (black circle) belonging to metric perturbations of opposite parities move apart in the complex frequency plane when the parameter  $\varepsilon$  is tuned from zero (“general relativity”) to a nonzero value. Only one pair of frequencies is shown in the figure; however, this split also occurs, not necessarily in the same way, for all other frequencies. In our problem,  $\varepsilon$  is related to the lengthscale  $l$  associated with higher-curvature terms in the EFT. Understanding how isospectrality breaking impacts the black-hole ringdown is the main goal of this paper.

black-hole spacetime we study. In Sec. III, we give a concise account of the two master equations that describe linear metric perturbations to this black hole and discuss their properties. Next, in Sec. IV, we carry out time-domain numerical simulations of these master equations. We study how different the resulting waveforms are from their general-relativistic limit and examine their spectral content. In Sec. V, we give a prescription for combining these waveforms to obtain the gravitational wave polarizations in the EFT and discuss what information can and cannot be extracted from them. In Sec. VI, we summarize our findings, discuss their limitations, and entertain some conjectures. The main text is supplemented by three appendices. In Appendix A, we describe our numerical code, and present convergence tests and error estimates. In Appendix B, we discuss how a wave equation with a variable propagation speed can be mapped into a wave equation with a constant propagation speed but with a modified effective potential. In Appendix C, we present additional simulations that explore the initial-data parameter space.

We use geometrical units  $c = G = 1$  and the mostly plus metric signature. We denote by  $l$  the lengthscale associated to higher-curvature corrections to general relativity,  $l^4$  being the order of the corrections we study. We work perturbatively to leading order in the dimensionless parameter  $\varepsilon = (l/M)^4$ , where  $M$  is the black hole’s mass.

## II. ACTION AND FIELD EQUATIONS

We consider the following action

$$S = \frac{1}{16\pi} \int d^4x \sqrt{-g} R + \frac{1}{16\pi} \sum_{n \geq 2} l^{2n-2} S^{(2n)}, \quad (1)$$

where  $l$  is a lengthscale assumed to be small compared to the lengthscale associated with a black hole of mass  $M$ , i.e.,  $M \gg l$ , and  $S^{(2n)}$  is the action of the  $n$ th order curvature term which has  $2n$  derivatives of the metric. We then call  $S^{(2n)}$  a ‘‘dimension- $2n$  operator.’’ Notice that only even powers in  $l$  are allowed by dimensional analysis.

As long as the EFT construction is built around vacuum general relativity and by performing field redefinitions, one can show that no dimension-four operator exists. The first nontrivial contribution occurs at dimension six and, at this order, there are only two operators [18, 19]. The resulting action is

$$S = \frac{1}{16\pi} \int d^4x \sqrt{-g} [R + l^4 \mathcal{L}], \quad (2)$$

where

$$\mathcal{L} = \lambda_e R_{\mu\nu}{}^{\rho\sigma} R_{\rho\sigma}{}^{\delta\gamma} R_{\delta\gamma}{}^{\mu\nu} + \lambda_o R_{\mu\nu}{}^{\rho\sigma} R_{\rho\sigma}{}^{\delta\gamma} \tilde{R}_{\delta\gamma}{}^{\mu\nu}. \quad (3)$$

Here,  $\tilde{R}_{\mu\nu\rho\sigma} = (1/2) \epsilon_{\mu\nu}{}^{\alpha\beta} R_{\alpha\beta\rho\sigma}$ ,  $\epsilon_{\mu\nu\rho\sigma}$  is the totally anti-symmetric Levi-Civita tensor, and  $\lambda_{e,o}$  are dimensionless constants associated to the even- (‘‘e’’) and odd-parity (‘‘o’’) curvature terms.

The field equations of the theory, obtained by varying the action (2) with respect to  $g^{\mu\nu}$ , are:

$$\mathcal{E}_{\alpha\beta} = G_{\alpha\beta} + l^4 \mathcal{S}_{\alpha\beta} = 0, \quad (4)$$

where

$$\mathcal{S}_{\alpha\beta} = P_{(\alpha}{}^{\rho\sigma\gamma} R_{\beta)\rho\sigma\gamma} - \frac{1}{2} g_{\alpha\beta} \mathcal{L} + 2\nabla^\sigma \nabla^\rho P_{(\alpha|\sigma|\beta)\rho}, \quad (5a)$$

$$P_{\alpha\beta\mu\nu} = 3\lambda_e R_{\alpha\beta}{}^{\rho\sigma} R_{\rho\sigma\mu\nu} + \frac{3}{2} \lambda_o (R_{\alpha\beta}{}^{\rho\sigma} \tilde{R}_{\rho\sigma\mu\nu} + R_{\alpha\beta}{}^{\rho\sigma} \tilde{R}_{\mu\nu\rho\sigma}). \quad (5b)$$

As in Ref. [17], we will only consider the even-parity operator; we set  $\lambda_o = 0$  and write  $\lambda_e = \lambda$ . We assume  $\lambda$  to be positive, though  $\lambda$  can have either sign a priori [20–22]. We will work to leading order in  $\lambda$ , that is, to  $\mathcal{O}(l^4)$ . Other aspects of the EFT in the context of gravitational-wave physics are discussed, for instance, in Refs. [23–32] and references therein.

In the presence of the dimension-six operators, the Schwarzschild solution is no longer a solution in the EFT. Yet, an analytical black hole solution that reduces to Schwarzschild when  $\lambda = 0$  can be found perturbatively. Its line element in Schwarzschild coordinates is

$$ds^2 = -N^2 f dt^2 + f^{-1} dr^2 + r^2 d\theta^2 + r^2 \sin^2 \theta d\phi^2, \quad (6)$$

where the metric functions  $N$  and  $f$  are

$$N^2 f = \left(1 - \frac{r_h}{r}\right) \left[1 - \varepsilon \left(\frac{5M}{8r} + \frac{5M^2}{4r^2} + \frac{5M^3}{2r^3} + \frac{5M^4}{r^4} + \frac{10M^5}{r^5} + \frac{20M^6}{r^6}\right)\right], \quad (7a)$$

$$f^{-1} = \left(1 - \frac{r_h}{r}\right)^{-1} \left[1 + \varepsilon \left(\frac{5M}{8r} + \frac{5M^2}{4r^2} + \frac{5M^3}{2r^3} + \frac{5M^4}{r^4} + \frac{10M^5}{r^5} - \frac{196M^6}{r^6}\right)\right]. \quad (7b)$$

We defined the perturbative parameter

$$\varepsilon = \lambda(l/M)^4, \quad (8)$$

where  $M$  is the hole’s Arnowitt–Deser–Misner mass, and  $r_h$  is the location of the event horizon,

$$r_h = 2M(1 - 5\varepsilon/16). \quad (9)$$

The black hole is of Petrov-type D [17]. All our calculations are carried out to leading order in  $\varepsilon$ .

### III. BLACK HOLE PERTURBATIONS

#### A. Review of the main equations

In Ref. [17], we studied the linear gravitational perturbations of the black hole solution (6) in the metric-based formalism pioneered by Regge, Wheeler, and Zerilli [7–9], following, in particular, the conventions from Martel and Poisson [33]. Our approach to this problem in the EFT differed in some aspects from that of Refs. [19, 34]. We refer the reader to Ref. [17], Sec. 3 for details.

In brief, the problem reduces to studying two wave equations:

$$[-c_s^{-2}(r)\partial_{tt} + \partial_{r_* r_*} - V_\ell^{(\pm)}(r)] X_\ell^{(\pm)}(t, r) = 0. \quad (10)$$

We use the superscript  $(\pm)$  to denote variables associated to metric perturbations of polar (+) or axial (−) parity, and label them by their multipolar index  $\ell \geq 2$ . Metric perturbations of polar and axial parities are completely described by a single master function known as the Zerilli–Moncrief (ZM)  $X^{(+)}$  and Cunningham–Price–Moncrief (CPM)  $X^{(-)}$  functions, respectively. These are close relatives of the Zerilli [8] and Regge–Wheeler functions [7], respectively. These two pairs of master functions satisfy the same *homogeneous* differential equations both in the EFT and in the limit of general relativity.

In Eq. (10), we also defined the tortoise coordinate  $r_*$

$$dr_*/dr = 1/(Nf), \quad (11)$$

which maps the domain  $r_h \leq r < \infty$  to  $-\infty < r_* < \infty$ . Details about the tortoise coordinate can be found in Ref. [17], Appendix D. Also in Eq. (10),  $c_s$  and  $V_\ell^{(\pm)}$  are the space-dependent propagation velocity of the perturbations and black-hole effective potentials, respectively. The former is given by [19]

$$c_s^2 = 1 - 288\varepsilon \left(1 - \frac{r_h}{r}\right) \frac{M^5}{r^5}. \quad (12)$$

Note that  $c_s$  approaches unity at the event horizon and spatial infinity. It also has a single extremum at  $r = 6r_h/5$ , at which the propagation speed deviates from unity by the amount

$$(1 - c_s^2)|_{r=6r_h/5} = \frac{3125}{162} \frac{M^5}{r_h^5} \varepsilon \simeq \frac{3125}{5184} \varepsilon \approx 0.603\varepsilon, \quad (13)$$

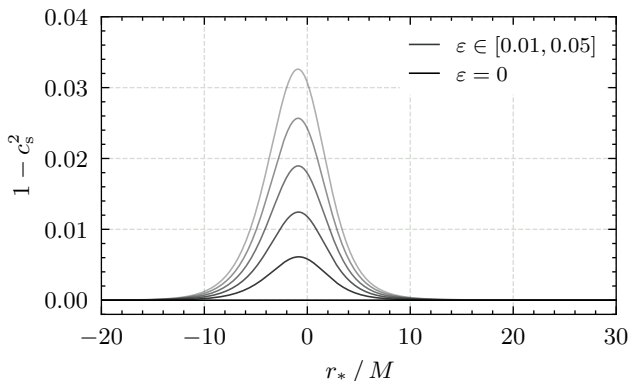


FIG. 2. Deviation from unity of the propagation speed squared of linear metric perturbations. We vary the parameter  $\varepsilon = \lambda l^4 / M^4$  from zero (general relativity) to 0.05 in increments of 0.01. The maximum deviation from the speed of light happens at  $r = 6r_h/5$ , near the hole's horizon  $r_h$ , and vanishes at the horizon and at spatial infinity.

to leading order in  $\varepsilon$ . The deviation can be super or subluminal depending on the sign of  $\varepsilon$  [19]. We consider the latter case only. Figure 2 shows the spatial profile of  $c_s^2$  in the range  $\varepsilon \in [0, 0.05]$  in increments of 0.01.

We write the effective potential as

$$V_\ell^{(\pm)} = \left(1 - \frac{r_h}{r}\right) \left[\bar{V}_\ell^{(\pm)} + \varepsilon \delta V_\ell^{(\pm)}\right]. \quad (14)$$

The general-relativistic contributions to the potential are the Zerilli [8] and Regge–Wheeler [7] potentials,

$$\bar{V}_\ell^{(+)} = \frac{1}{(r\Lambda_\ell)^2} \left[ 2\lambda_\ell^2 (\Lambda_\ell + 1) + \frac{18M^2}{r^2} \left( \lambda_\ell + \frac{M}{r} \right) \right], \quad (15a)$$

$$\bar{V}_\ell^{(-)} = \frac{1}{r^2} \left[ \ell(\ell + 1) - \frac{6M}{r} \right], \quad (15b)$$

respectively, where we defined:

$$\lambda_\ell = (\ell + 2)(\ell - 1)/2, \quad \text{and} \quad \Lambda_\ell = \lambda_\ell + 3M/r. \quad (16)$$

The modifications to these potentials originating from the cubic-in-curvature terms have the form

$$\delta V_\ell^{(+)} = \frac{1}{(r\Lambda_\ell)^2} \sum_{k=1}^{10} v_{k\ell}^{(+)}(r) \left( \frac{M}{r} \right)^k, \quad (17a)$$

$$\delta V_\ell^{(-)} = \frac{1}{r^2} \sum_{k=1}^7 v_{k\ell}^{(-)} \left( \frac{M}{r} \right)^k. \quad (17b)$$

The coefficients  $v_{k\ell}^{(+)}$  depend on  $\Lambda_\ell$  for  $k > 4$ , hence their dependence on  $r$ . In contrast, the coefficients  $v_{k\ell}^{(-)}$  are independent of  $r$  for all  $k$ . The explicit form of  $v_{k\ell}^{(\pm)}$  can be found in Ref. [17], Appendix E.<sup>1</sup> Figure 3 shows

<sup>1</sup> A cautionary note: the coefficients  $v_{k\ell}^{(+)}$  for the corrections to the Zerilli potential contain a typo in Ref. [17]; all coefficients therein should be divided by four.

the spatial profile of  $V_2^{(\pm)}$  in the range  $\varepsilon \in [0, 0.05]$  in increments of 0.01.

The  $\varepsilon$  corrections to the Zerilli and Regge–Wheeler potentials break the equivalence between quasinormal-frequency spectrum of metric perturbations of polar and axial parity that exists in general relativity [10–12]. The breakdown of isospectrality was first found through numerical calculations in Refs. [19], and its origin was discussed through the analysis of a hierarchy of integral identities in Ref. [17]; see also Refs. [35, 36]. A particular EFT of general relativity involving quartic-in-curvature terms that preserves isospectrality in the geometrical optics (eikonal) limit was identified in Ref. [15] and explored in Ref. [37].

We notice that Ref. [38] studied Eq. (10) using a hyperboloidal foliation of spacetime, whereas Ref. [39] considered the equivalent of Eq. (10) in the quartic-in-curvature EFT of general relativity using double null coordinates.

## B. First-order form of the wave equation and initial data

We solve Eq. (10) using momentarily static initial data:

$$\partial_t X_\ell^{(\pm)}|_{t=0} = 0, \quad (18)$$

with compact support, localized far from the black hole. In particular, we assume that  $X_\ell^{(\pm)}$  has a Gaussian spatial profile at  $t = 0$ ,

$$X_\ell^{(\pm)}|_{t=0} = A e^{-(r_* - r_*^{\text{med}})^2 / (2\sigma^2)}, \quad (19)$$

of width  $\sigma$ , amplitude  $A$ , and centered at  $r_*^{\text{med}} \gg r_h$ . In all our simulations, we chose

$$A = 1, \quad \sqrt{2}\sigma = 1.5M, \quad \text{and} \quad r_*^{\text{med}} = 100M. \quad (20)$$

We rewrite Eq. (10), for each parity ( $\pm$ ) and multipole  $\ell$ , as a system of first-order-in-time coupled partial differential equations. For brevity, in the remainder of this subsection, we omit the scripts ( $\pm$ ) and  $\ell$ . We perform the order reduction by introducing the auxiliary variables

$$\Pi = \partial_t X, \quad \text{and} \quad \Psi = \partial_{r_*} X. \quad (21)$$

The system of equations that follows from Eq. (10) is then

$$\partial_t \Pi = c_s^2 (\partial_{r_*} \Psi - V X), \quad (22a)$$

$$\partial_t \Psi = \partial_{r_*} \Pi, \quad (22b)$$

$$\partial_t X = \Pi. \quad (22c)$$

We evolve these equations forward in time using the method of lines. The waveforms are extracted from the value of  $X(t, r_*^{\text{ext}})$  at an extraction radius  $r_*^{\text{ext}} = 150M$ . Specifically, our code uses finite-difference stencils that are fourth-order accurate in space and evolves the variables in time using the third-order accurate Runge–Kutta scheme of Shu and Osher [40]. Details of our code are described in Appendix A, where we also discuss the code's numerical convergence and give error estimates on our waveforms.

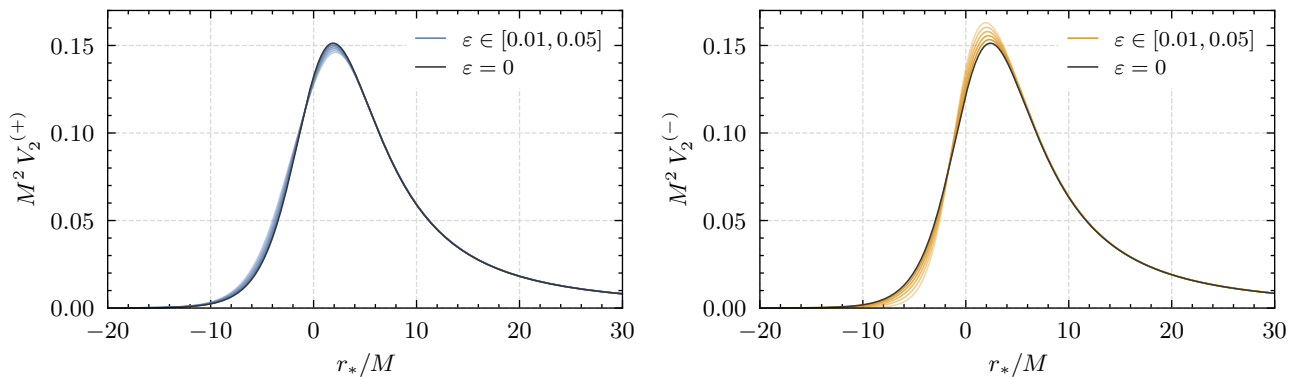


FIG. 3. The effective potentials  $V_2^{(\pm)}$  for perturbations of polar (left panel) and axial (right panel) parity. We vary the parameter  $\varepsilon = \lambda t^4/M^4$  from zero (general relativity) to 0.05 in increments of 0.01. Deviations from general relativity are mostly bound to the region between the event horizon, pushed to  $r_* \rightarrow -\infty$ , and the location of the potential peak.

#### IV. NUMERICAL RESULTS

We largely explored the quadrupole perturbations of axial and polar parity. We begin by revisiting the Vishveshwara’s scattering experiments in general relativity in Sec. IV A, and go beyond Einsteinian theory in Sec. IV B. In the latter case, we first study the effect of the variable propagation speed on the evolution of the perturbations and how we can map this problem into a wave equation with a constant propagation speed but with a modified effective potential in Sec. IV B 1. We discuss how the waveforms in the EFT differ from those in general relativity in Sec. IV B 2, and study their spectral content in Sec. IV B 3. We do so by extracting the fundamental quasinormal frequency through a fitting procedure, which we compare against previous frequency domain calculations.<sup>2</sup>

##### A. General relativity

Surprisingly, we have not found in the literature a scattering experiment done with the Zerilli potential, with the exception of the somewhat related work [43]. It seems that since Vishveshwara [1] the literature has used the Regge–Wheeler potential exclusively. An “exception” is Press, who performed time evolutions in the large- $\ell$  limit [2]. In this limit, however, the Regge–Wheeler and Zerilli potentials become identical.

For the sake of completeness, we present such a comparison in Fig. 4. We show the polar (solid line) and

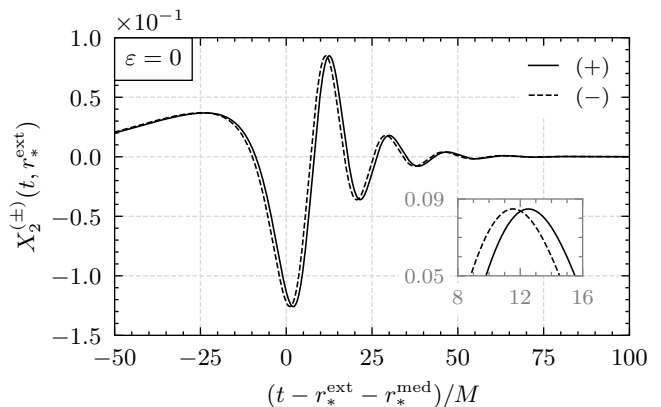


FIG. 4. Quadrupolar axial- and polar-parity waveforms in general relativity obtained by evolving the same initial data. The inset zooms near the peak of the waveforms and shows that they are offset by approximately  $M$ .

axial-parity (dashed line) waveforms obtained by evolving the same initial data described in Sec. III B. The abscissa has been shifted by the extraction radius,  $r_*^{\text{ext}} = 150M$ , and the median position of the initial data,  $r_*^{\text{med}} = 100M$ . The two waveforms are exquisitely similar to each other, except for a shift in time of approximately  $1M$ . This is most easily seen in the inset, wherein we zoom around a peak of the waveforms. We attribute this difference to the different travel times required by the same initial Gaussian wave packet to reach the peak of the effective potential  $V_2^{(\pm)}$ . These peaks differ by approximately  $M$ , occurring at larger values of  $r_*$  for the Regge–Wheeler potential than for the Zerilli potential. This causes the axial-parity waveform to arrive at  $r_*^{\text{ext}}$  slightly earlier than its polar-parity counterpart. Shifting both waveforms in time according to their maximum value of  $|X_2^{(\pm)}|$  makes both virtually indistinguishable. For this reason, wherever we show a waveform in general relativity in the next sections, we have arbitrarily chosen to show the axial-parity waveform. We note that Cunningham et al. [44, 45] also

<sup>2</sup> We remark that to our knowledge, the first time-domain analysis on isospectrality breaking was done by Chaverra et al. [41] in the context of linear perturbations of nonrotating black holes in nonlinear electromagnetism. The isospectrality of the quasinormal mode spectra of axial and polar perturbations of the Reissner–Nordström solution, shown by Chandrasekhar [42], is generally broken in these nonlinear extensions to Maxwell’s theory.

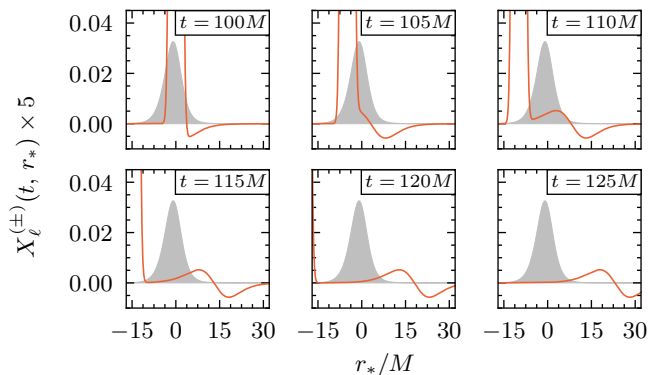


FIG. 5. Snapshots of the incident perturbation (solid line and rescaled by a factor of 5) as it propagates into the region of variable propagation speed. The filled gray curve represents  $1 - c_s^2$ , for  $\varepsilon = 0.05$ , as also shown in Fig. 2. As the left-moving perturbation reaches the region in which  $c_s^2$  deviates from one, part of it is reflected, as shown in the top panels. This reflected pulse propagates rightward (see the bottom panels) and is measured by an observer at  $r_*^{\text{ext}}$  as the waveforms in Fig. 6.

observed the similarity between waves of both parities in the perturbed Oppenheimer–Snyder collapse [46].

## B. Beyond general relativity

After this brief discussion about waveforms in general relativity, we now consider nonzero values of  $\varepsilon$ .

### 1. Effects of the variable propagation speed

We first study the effects of  $c_s^2$  on the waveforms. To isolate the effects produced by this term, we begin by artificially setting the potentials  $V_\ell^{(\pm)}$  equal to zero in the wave equation (10) and chose  $\varepsilon = 0.05$  to maximize the effects of  $c_s^2$ . Because the potentials are zero, the resulting evolution is identical for perturbations of axial and polar parity and is independent of  $\ell$ . With this setup, we followed the evolution of the incident pulse as it entered the region of space in which  $c_s^2$  deviates the most from one. Figure 5 shows a sequence of snapshots of the evolution. Specifically, we show the incident perturbation (solid line, rescaled by a factor of 5) as it propagates into the region of variable speed. This region is represented in the figure by the filled curve superimposed in each panel; cf. Fig. 2. As the pulse enters this region, part of it is reflected. The bulk of the incident pulse then continues moving leftward, and a second reflection occurs when the bulk of the incident pulse leaves the region in which  $c_s$  is not one. Eventually, the bulk of the pulse falls into the hole, leaving behind a double-peaked wave that propagates to spatial infinity.

To understand how  $\varepsilon$  influences the amplitude of the reflected wave, we varied  $\varepsilon$  from 0.01 to 0.05 in increments

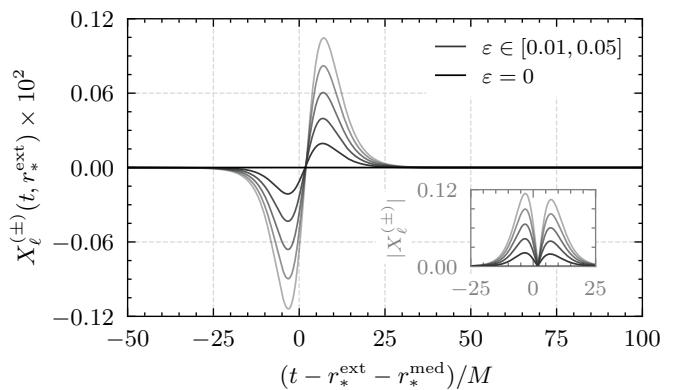


FIG. 6. Waveforms with varied  $\varepsilon$  obtained by artificially setting the effective potential  $V_\ell^{(\pm)}$  to zero while maintaining a variable  $c_s^2$ . The amplitude of the reflected wave grows with increasing  $\varepsilon$ , i.e., with the increasing deviation from unit of  $c_s^2$ ; see Fig. 2. In each waveform, the peak that arrives first has larger absolute value than the second, as shown in the inset. The asymmetry is due to the asymmetry of  $c_s^2$  with respect to the location of this maxima.

of 0.01. Figure 6 shows the results of this exercise. We show the waveforms extracted at a location  $r_*^{\text{ext}}$  far away from the hole. Unsurprisingly, the amplitude of the reflected perturbation increases with  $\varepsilon$ . Through a curve fit, we find that maximum amplitude scales linearly with  $\varepsilon$ , as expected, and is well approximated by

$$\max |X_\ell^{(\pm)}| \simeq 0.022460 \varepsilon, \quad (23)$$

for the initial data and in the range of  $\varepsilon$ -values we studied. This is approximately 5% of the amplitude of the incident perturbation. The structure of the scattered wave exhibits a small (but visible by eye) asymmetry. This is most easily seen by plotting the absolute value of the wave, as we do in the inset. The asymmetry is a consequence of the asymmetry of  $c_s^2$  with respect to its maximum; cf. Fig. 2.

How much does the variable propagation speed contribute to the final waveform when we include the effective potential in our simulations? To answer this question, we performed a second suite of simulations, evolving both axial and polar-parity quadrupolar  $\ell = 2$  perturbations where we varied  $\varepsilon$  from 0.01 to 0.05 in increments of 0.01 and artificially set  $c_s^2 = 1$ , but including  $V_\ell^{(\pm)}$ . Next, we ran a third set of simulations, but now including the effect of  $\varepsilon$  on both  $c_s^2$  and in the potentials; that is, we evolved the complete Eq. (10). Together with the simulations discussed in Figs. 5 and 6, we thus have three sets of simulations that we label as cases (a), (b), and (c), as summarized below:

- (a)  $c_s^2 \neq 1$  and  $V_\ell^{(\pm)} \neq 0$ ,
- (b)  $c_s^2 = 1$  and  $V_\ell^{(\pm)} \neq 0$ ,
- (c)  $c_s^2 \neq 1$  and  $V_\ell^{(\pm)} = 0$ .

In Fig. 7, we show an illustrative waveform of each case, namely, for quadrupolar axial perturbations and  $\varepsilon = 0.05$ .

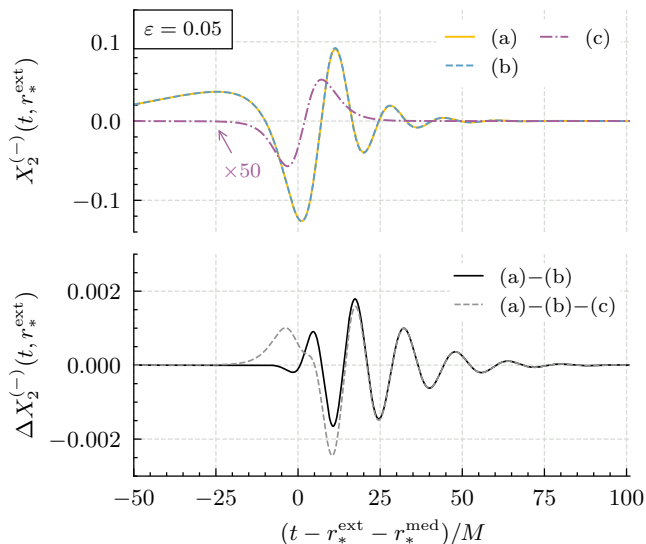


FIG. 7. Comparison between quadrupolar axial waveforms calculated when we set in the wave equation (10): (a)  $c_s^2 \neq 1$  and  $V_\ell^{(\pm)} \neq 0$ , (b)  $c_s^2 = 1$  and  $V_\ell^{(\pm)} \neq 0$ , and (c)  $c_s^2 \neq 1$  and  $V_\ell^{(\pm)} = 0$ . We consider  $\varepsilon = 0.05$  in all cases. In the top panel, we show the three waveforms. We see that the effects of the variable propagation speed on the waveform are subdominant relative to the presence of the effective potential; compare the waveforms (a) and (b), and their amplitude relative to the waveform (c), which we rescaled by a factor of 50. In the bottom panel, we subtract from the complete solution of Eq. (10), the result of (b) (solid line) and the sum of cases (b) and (c) (dashed line).

In the top panel, we plot the three waveforms for case (a) (solid line), (b) (dashed line) and (c) (dot-dashed line), rescaled by a factor of 50. We find that the contribution of  $c_s^2$  is small [compare the waveforms for cases (a) and (b)] and subdominant relative to the contribution of the effective potential [compare the waveforms for case (c) against those of cases (a) and (b)]. In the bottom panel, we show the difference between the “complete” waveform (a) to case (b) (solid line) and when we subtract from (a) the sum of waveforms of cases (b) and (c) (dashed line). We see that the differences are  $\mathcal{O}(10^{-3})$ , comparable to the order of magnitude of the waveform corresponding to case (c), shown in Fig. 6. These observations are also shared by the polar-parity perturbations.

Before closing this section, we remark that the variable-speed wave equation (10) can be recast as a constant-speed wave equation [47],

$$[-\partial_{tt} + \partial_{\tilde{r}\tilde{r}} - W_\ell^{(\pm)}(r)] Y_\ell^{(\pm)}(t, r) = 0, \quad (24)$$

for new master functions  $Y_\ell^{(\pm)}$ , coordinate  $\tilde{r}$ , and effective potential

$$W_\ell^{(\pm)} = c_s^2 V_\ell^{(\pm)} - \{r_*, \tilde{r}\}, \quad (25)$$

where  $\{r_*, \tilde{r}\}$  is the Schwarzian derivative defined as

$$\{x, y\} = \frac{1}{2} \frac{d}{dy} \left( \frac{\ddot{x}}{\dot{x}} \right) - \frac{1}{4} \left( \frac{\dot{x}}{\dot{x}} \right)^2, \quad \dot{x} = dx/dy. \quad (26)$$

We present the derivation of Eq. (24), discuss the properties of  $W_\ell^{(\pm)}$ , and report the result of an illustrative simulation (as well as of an unsolved puzzle) in Appendix B. Hereafter, we use Eq. (10) for our simulations.

## 2. Waveform comparison

We now focus exclusively on the waveforms in case (a), the solutions to Eq. (10), and compare them against their general-relativistic counterparts. We begin by considering  $\varepsilon = 0.05$ , the largest value of  $\varepsilon$  we considered.

In Fig. 8, we show the quadrupolar waveforms  $X_2^{(\pm)}$  in logarithmic scale. We shifted the abscissa such that the time instant  $t_{\text{peak}}$  at which the maximum (absolute) value of the waveform occurs is zero. The three curves represent the cases of general relativity (solid line), and polar (dashed line) and axial (dot-dashed line) perturbations in the effective field theory with  $\varepsilon = 0.05$ . After doing this alignment in time, we see that all three waveforms are very similar initially. They start to become visually different as we enter the “ringdown” stage that is dominated by the quasinormal frequencies of the black hole. After these frequencies have been sufficiently damped, the signal is dominated by a power-law tail that is identical for the three waveforms. Because the damping of the quasinormal frequencies of polar and axial perturbations is shifted differently by  $\varepsilon$ , the power-law tail of the respective waveforms become prominent at different times. Specifically, it occurs later for the polar perturbations in comparison

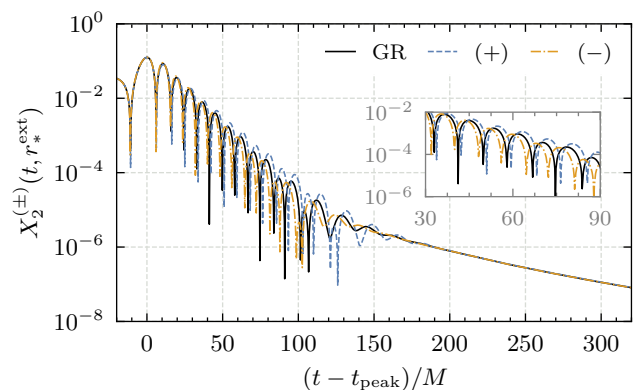


FIG. 8. Comparison between waveforms in general relativity and in the effective field theory. The solid line corresponds to the CPM waveform in general relativity (“GR”), while the dashed and dot-dashed lines represent the ZM, “(+)” and CPM, “(-)” waveforms when  $\varepsilon = 0.05$ . The waveforms were shifted in time such that their peaks occur at zero. The inset shows the waveforms in a time interval in which the signal is dominated by the quasinormal frequencies of the black hole.

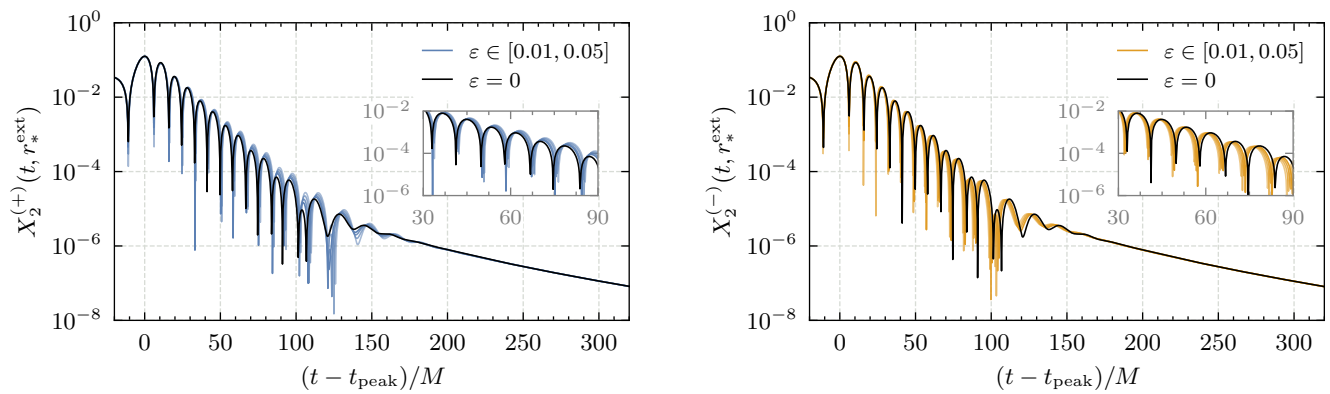


FIG. 9. Comparison between waveforms in general relativity and in the effective field theory for various values of  $\varepsilon$ . The solid line corresponds to the parity odd waveform in general relativity, while the blue and orange lines represent the even-parity (left panel) and odd-parity (right panel) waveforms for  $\varepsilon \in [0, 0.05]$  in increments of 0.01. As in Fig. 8, the inset shows the waveforms in a time interval in which the signal is dominated by the quasinormal frequencies of the black hole.

to the axial perturbations. In the inset, we zoom into the waveforms' ringdown. Qualitatively, we see two trends. First, the oscillation frequency increases (decreases) for the axial (polar) waveform with respect to general relativity. Second, the damping of the oscillations is faster (slower) for the axial (polar) waveform with respect to general relativity. These are the expected outcomes from the frequency-domain calculations of the fundamental quasinormal frequency carried out in Ref. [17]. We will do a quantitative comparison between the spectral content of our waveforms against these frequency-domain results in Sec. IV B 3.

Figure 9 is similar to Fig. 8 except that we include intermediate values of  $\varepsilon$  from zero up to 0.05 in steps of 0.01. To reduce visual clutter, we separate the even- and odd-parity waveforms into the left and right panels, respectively. As expected, waveforms with smaller values of  $\varepsilon$  are more similar to the general-relativistic waveform, while the differences share the general trends shown in Fig. 8 for  $\varepsilon = 0.05$ . Finally, we see after  $t$  approximately  $180M$  after the peak, all waveforms exhibit the same power-law tail behavior.

### 3. Spectral content of the waveforms

Having gained some understanding of the different ingredients that make up our waveforms, we now study them in more detail. In particular, we address two items. First, we study their spectral content. In particular, we extract the quasinormal frequencies in the signals and compare them against our previous frequency-domain calculations [17]. Second, we provide a quantitative measure of how much the waveforms differ from those in the limit of general relativity. We address these questions at the level of the metric-perturbation master functions  $X^{(\pm)}$  in this section. In Sec. V, we will discuss the observational prospects of the results obtained herein by relating  $X^{(\pm)}$  to the gravitational wave polarizations.

Let us begin with the quasinormal frequencies. Here, we follow Ref. [48]; see also Refs. [49, 50]. A comprehensive review of quasinormal-frequency extraction strategies can be found in Ref. [6]. We use as our fitting model for the  $(\ell, m)$  multipole of the waveform a linear superposition of damped sinusoids:

$$Q_N = \sum_{n=0}^N A_n e^{-\omega_{i,n}(t-t_{\text{peak}})} \sin[\omega_{r,n}(t-t_{\text{peak}}) + \phi_n], \quad (27)$$

where  $N$  denotes the number  $n$  of overtones in the model,  $A_n$  their amplitude,  $\omega_{i,n} = \text{Im} \omega_{\ell n}$ ,  $\omega_{r,n} = \text{Re} \omega_{\ell n}$ , and  $\phi_n$  a phase. The fit is applied to our numerical data in a time window

$$t \in [t_0, t_{\text{end}}], \quad (28)$$

where  $t_0$  and  $t_{\text{end}}$  are measured with respect to  $t_{\text{peak}}$ . Based on the conclusions of Refs. [48, 49], we focus on extracting the fundamental quasinormal frequency only; i.e., we use  $N = 0$ . For this reason, we omit the subscript  $n$  hereafter.

To perform our fits, we keep  $t_{\text{end}} = 90M$  fixed, while allowing  $t_0$  to vary in the interval  $t_0 \in [0, 30]M$  in steps of  $1M$ ; see Fig. 10 for an illustration. We found that our results are insensitive to shifting  $t_{\text{peak}}$  up to  $120M$ . For each time window, we fit Eq. (27) against the numerical data using the `curve_fit` function from SciPy [51] to perform a least-square fitting. We use the ‘‘Trust Region Reflective’’ algorithm and set the bounds

$$A \in [0, 1], \quad \phi \in [0, 2\pi), \quad \omega_r \in [0, 2\omega_r^{\text{GR}}], \quad \omega_i \in [0, 2\omega_i^{\text{GR}}],$$

on the free parameters of  $Q_0$ . Here,  $\omega_{r,i}^{\text{GR}}$  are the real and imaginary parts of the fundamental quasinormal frequency of a Schwarzschild black hole [10]. For  $\ell = 2$ , they are

$$M\omega_r^{\text{GR}} = 0.373671, \quad \text{and} \quad M\omega_i^{\text{GR}} = -0.0889623. \quad (29)$$

We initialize the fitting algorithm by giving each free model parameter a random initial guess, by drawing a

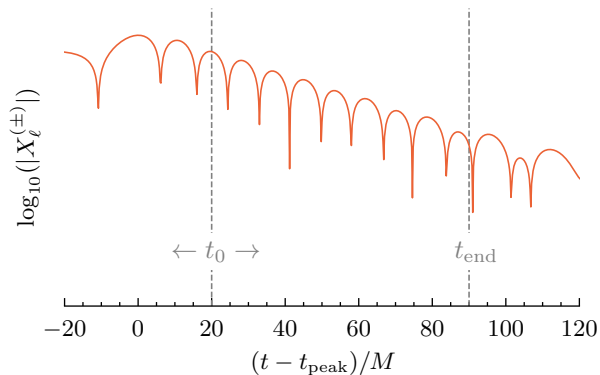


FIG. 10. Illustration of the variable time window in which we perform our fits. We vary the initial time  $t_0$  in the interval  $t_0 \in [0, 30]M$ , measured with respect to the time instant in which the waveform has its largest value,  $t_{\text{peak}}$ . The end time is fixed to  $t_{\text{end}} = 90M$ .

sample from a uniform probability distribution within the bounds on our parameters [49].

We repeat this fitting process 100 times for each value of  $t_0$  to allow the algorithm to converge to the true minima. We then select from these 100 fits the tuple of best-fit parameters that gives the smallest mismatch  $\mathcal{M}$  between model and numerical data. Consider two signals  $h_{1,2}(t)$ . We define their inner product in the time interval  $t \in [t_0, t_{\text{end}}]$  as

$$\langle h_1 | h_2 \rangle = \int_{t_0}^{t_{\text{end}}} dt h_1(t) h_2^*(t), \quad (30)$$

where the asterisk denotes complex conjugation. For our purposes the complex conjugation in Eq. (30) is inconsequential because our waveforms are real valued. We then define the mismatch  $\mathcal{M}$  as,

$$\mathcal{M} = 1 - \frac{\langle h_1 | h_2 \rangle}{\sqrt{\langle h_1 | h_1 \rangle \langle h_2 | h_2 \rangle}}. \quad (31)$$

Note that  $\mathcal{M} = 0$  if the waveforms are identical,  $h_1 = h_2$ . However, one must keep in mind that a small mismatch does not necessarily imply a good fit to the data. For example, if  $h_1$  and  $h_2$  differ by a nonzero multiplicative factor, their mismatch will be zero. Moreover, a small mismatch does not exclude the possibility that some parameters in the fitting model are overfitting the data; see Refs. [48, 49] for a discussion in the context of linear perturbation theory.

Figure 11 shows our results from applying this fitting process to  $X_2^{(\pm)}$ . We show the trajectories in the complex plane of the best-fit fundamental quasinormal frequency as we vary  $t_0 = t - t_{\text{peak}}$  from zero to  $30M$ . The plot is somewhat busy, so let us focus for the moment on the solid line labeled “GR,” for “general relativity.” Each circle along this curve represents a best-fit value of  $\omega_{20}$  for a given value of  $t_0$ . As  $t_0$  increases, the trajectory moves from left to right, looping around  $\text{Re}(M\omega_{20}) \approx 0.37$ . The

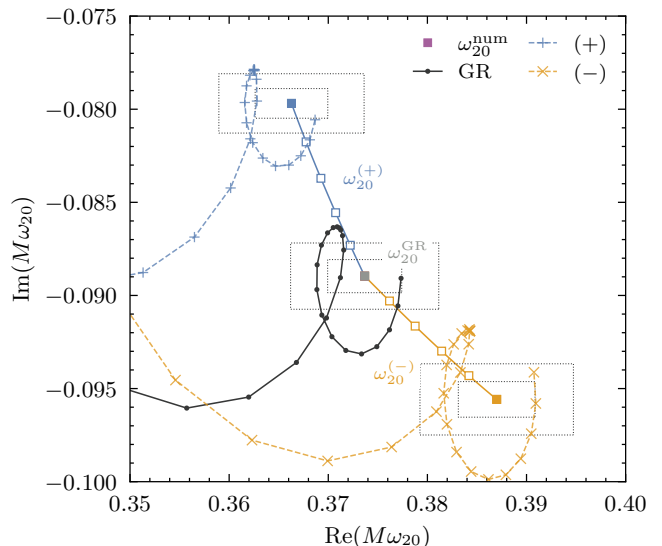


FIG. 11. Trajectories in the complex plane for the best-fit fundamental quasinormal frequencies  $\omega_{20}$  as  $t_0$  varies from zero to  $30M$ . The solid squares represent the frequencies calculated by us in Ref. [17]. The solid square at the center of the figure indicates  $\omega_{20}$  of a Schwarzschild black hole, (29), and that has the same value for axial and polar perturbations. This degeneracy is broken by nonzero values of  $\varepsilon$ . As we increase this parameter, the polar (axial) quasinormal frequency moves upward (downward) in the complex frequency plane, as indicated by the solid lines; intermediate values of the frequencies for  $\varepsilon = 0.01, 0.02, 0.03$  and  $0.04$  are indicated by empty squares. The two curves terminate at  $\varepsilon = 0.05$ , and we indicate the frequency values, cf. Eq. (32), with the two additional solid squares. The dotted-lined rectangles represent  $\pm 1\%$  and  $\pm 2\%$  away from these frequencies. We see that as  $t_0$  approaches  $30M$ , the best-fit frequencies approach their expected values determined by the frequency-domain calculation of Ref. [17].

trajectory then approaches the true value (29), indicated by a filled square, as  $t_0$  approaches  $30M$ . The dotted-lined rectangles represent values  $\pm 1\%$  and  $\pm 2\%$  away from (29).

We now move away from the general-relativity curve by increasing  $\varepsilon$ . A nonzero value of  $\varepsilon$  breaks the degeneracy between  $\omega^{(+)}$  and  $\omega^{(-)}$  that exists in general relativity. Figure 11 shows this through the curves that branch up and downward from the Schwarzschild frequency. The curves terminate at  $\varepsilon = 0.05$ , for which

$$M\omega_{20}^{(+)} = 0.366287 - 0.0796875i, \quad (32a)$$

$$M\omega_{20}^{(-)} = 0.386990 - 0.0955811i. \quad (32b)$$

Quasinormal frequencies corresponding to the intermediate values of  $\varepsilon = 0.01, 0.02, 0.03$ , and  $0.04$  are indicated by the open squares. For “internal consistency,” these values are quoted from our previous work [17]; they agree to a few percent with the earlier works by de Rham et al. [19] and Cano et al. [34]. See Ref. [17], Fig. 3, in particular. We applied the fitting procedure to the waveforms for  $\varepsilon = 0.05$ . The best-fit values for  $\omega_{20}$  are shown by the

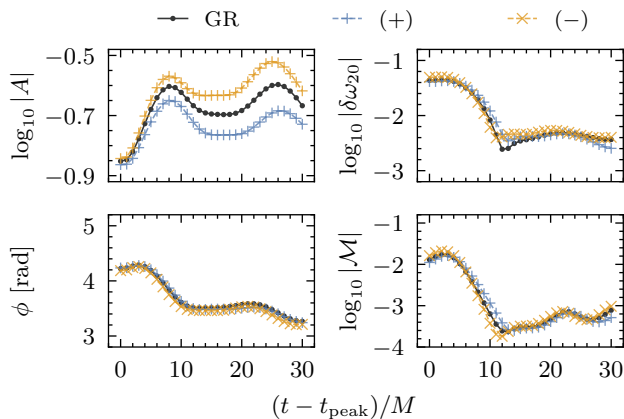


FIG. 12. Dependence of the mismatch and the best-fit parameters in our fitting model (27) as a function of  $t_0$  for the three waveforms shown in Fig. 8. We see that the absolute errors  $\delta\omega_{20}$  between the extracted frequencies and their reference values become nearly constant for  $t_0 \gtrsim 10M$ , and are smaller than 1%.

dashed lines. Different markers distinguish the polar and axial frequencies as described in the figure’s legend. The trajectories are similar to the case of general relativity. Satisfyingly, we were able to extract from our waveforms the values in Eq. (32) to 2% precision when  $t_0 = 30M$ .

We note the potential degeneracy between general relativity and the effective field theory depending on the time window used. Figure 11 shows that the general-relativity curve intersects the nonzero- $\varepsilon$  curve. This occurs for  $t_0 \approx 29M$ . Moreover, we see that depending on the value of  $t_0$ , the nonzero- $\varepsilon$  curves for  $\varepsilon = 0.05$  can intersect the exact values of  $\omega_{20}$  for *other* values of  $\varepsilon$ .

In Fig. 12, we show the mismatch  $\mathcal{M}$  and best-fit values of the parameters in our model  $Q_0$  as a function of  $t_0$  for the three waveforms we are analyzing. Specifically, we show the best-fit amplitude  $A$  (top left panel), absolute error in the quasinormal frequency  $\delta\omega_{20}$  (top right panel), phase  $\phi$  (bottom left panel), and mismatch  $\mathcal{M}$  (bottom right panel). Explicitly,

$$\delta\omega_{20} = |\omega_{20}^{\text{best-fit}} - \omega_{20}^{\text{num}}|, \quad (33)$$

where  $\omega_{20}^{\text{num}}$  is either numerical values (29) or (32), depending on the case. The curves are similar, both in their qualitative behavior and in magnitude. A notable difference is in the amplitude  $A$ , which increases (decreases) with respect to the general-relativity curve for the axial (polar) waveform starting around  $t_0 \gtrsim 6M$ . We attribute this behavior to the different damping times of the modes. Lastly, we see that the mismatch stabilizes for  $t_0 \gtrsim 10M$ , although it slowly increases around  $30M$  after  $t_{\text{peak}}$ .

We also calculated the mismatch (31) between our waveforms in the EFT with respect to general relativity for different values of  $\varepsilon$  as a function of  $t_0$ . To perform this calculation, we first aligned our nonzero- $\varepsilon$  waveforms with the peak of the general relativistic one. Then we evaluated the inner product (30), varying  $t_0 \in [-20, 200]M$  in

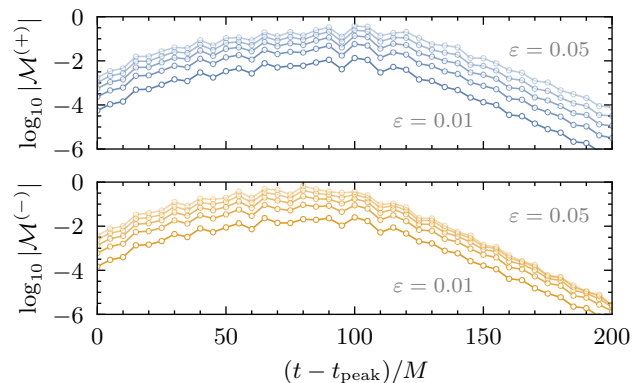


FIG. 13. Mismatch between polar (top panel) and axial (bottom panel) waveforms with respect to general relativity as a function of beginning of the time window  $t_0$ . The curves are similar, irrespective of the value of  $\varepsilon$ . However, unsurprisingly, they shift toward larger values of  $\mathcal{M}$  as  $\varepsilon$  increases. Focusing on the dependence on  $t_0$ , we see that  $\mathcal{M}$  is largest when the time interval contains the ringdown. As  $t_0 \gtrsim 150M$ , the time window contains mostly the power-law tail and the mismatches rapidly decrease; see Fig. 9.

increments of  $5M$  while keeping  $t_{\text{end}} = 230M$  fixed. We show the results of this exercise in Fig. 13. The behavior of the curves as a function of  $t_0$  is qualitatively the same for different values of  $\varepsilon$ . Increasing  $\varepsilon$  causes the mismatches to increase, as expected [38]. At fixed value of  $\varepsilon$ , we see that the mismatches increase with increasing  $t_0$ ; i.e., by having mostly the “ringdown-plus-tail” part of the waveforms in the inner product (30). Increasing  $t_0$  further makes the inner product involve mostly the tail portion of the signals and the mismatches decrease.

In Appendix C, we show the outcome of performing this fitting exercise to a small suite of simulations where the median  $r_*^{\text{med}}$  of our initial data is shifted. The upshot of our discussion therein is that we are able to extract more accurately the quasinormal frequencies the closer we make  $r_*^{\text{med}}$  to the peak of effective potential.

## V. OBSERVATIONAL IMPLICATIONS

So far we have studied the properties of the waveforms  $X^{(\pm)}$ . However, to make connection with gravitational-wave observables, we have established a relation between the ZM and CPM functions with the gravitational wave polarizations  $h_{+, \times}$ . In particular, we are interested in examining what happens when the even- and odd-parity ringdown waveforms, each dominated by their own respective fundamental quasinormal frequencies  $\omega_{20}^{(+)}$  and  $\omega_{20}^{(-)}$ , respectively, are combined to produce  $h_{+, \times}$ . How does, for instance,  $h_+$  behave, in comparison to general relativity, when we have two distinct fundamental quasinormal frequencies  $\omega_{20}^{(\pm)}$ ? Are we able to extract the frequencies  $\omega_{20}^{(\pm)}$  from this  $h_+$  as we accomplished in Sec. IV B 2 from  $X^{(\pm)}$ ? We investigate these questions next.

### A. Gravitational wave polarizations

In the context of general relativity, as discussed in Ref. [33], the gravitational wave polarization  $h_+$  and  $h_\times$  at future null infinity are related to the ZM and CPM master functions as

$$r h_+ = \sum_{\ell m} \left\{ X_{\ell m}^{(+)} \left[ \frac{\partial^2}{\partial \theta^2} + \frac{1}{2} \ell(\ell+1) \right] Y_{\ell m} - X_{\ell m}^{(-)} \frac{im}{\sin \theta} \left[ \frac{\partial}{\partial \theta} - \frac{\cos \theta}{\sin \theta} \right] Y_{\ell m} \right\}, \quad (34a)$$

$$r h_\times = \sum_{\ell m} \left\{ X_{\ell m}^{(+)} \frac{im}{\sin \theta} \left[ \frac{\partial}{\partial \theta} - \frac{\cos \theta}{\sin \theta} \right] Y_{\ell m} - X_{\ell m}^{(-)} \left[ \frac{\partial^2}{\partial \theta^2} + \frac{1}{2} \ell(\ell+1) \right] Y_{\ell m} \right\}, \quad (34b)$$

where  $Y_{\ell m}$  are spherical harmonics, while  $r$  corresponds to the distance to the black hole. In our case,  $r = r_{\text{ext}}$ .

How does the EFT affect this result? Because the EFT corrections to the propagation speed of the perturbations [cf. Eq. (12)] and effective potentials [cf. Eq. (17)] are only significant in the near horizon region, *Equation (34) holds in the EFT as well; all imprints of the EFT corrections are encoded in the master functions  $X_{\ell m}^{(\pm)}$  evaluated at future null infinity after they have scattered off the EFT-corrected potential barrier.* We verified that this is the case by inspecting the field equations in the limit of large  $r$ , where one recovers the result of general relativity [33].

### B. Synthetic signal generation: a toy model

Is there a way of using the results of Sec. IV to obtain the gravitational-wave polarizations? In a self-consistent calculation, each multipole  $X_{\ell m}^{(\pm)}$  would be computed by solving the inhomogeneous version of Eq. (10) with the right-hand side of these equations being given source terms that are responsible for driving the perturbations. For example, these source terms could represent a particle plunging in geodesic motion into the black hole, as studied in the classic papers by Davis et al. [52–54] in the 1970s, among others. We leave this ongoing calculation in the EFT to a forthcoming paper in this series [55].

Instead, for an initial study, we will make three assumptions that will enable us to use the results from Sec. IV. First, because of the spherical symmetry of our simulations in Sec. IV, we will assume that our waveform  $X_{\ell m}^{(\pm)}$  was obtained as if we had evolved a momentarily static initial data with Gaussian profile:

$$X_{\ell m}^{(\pm)} \Big|_{t=0} = A_{\ell m} e^{-(r_* - r_*^{\text{med}})^2 / (2\sigma^2)} \cos(m\phi), \quad (35)$$

where  $A_{\ell m}$  is the amplitude. Spherical symmetry guarantees that the dependence on the azimuthal angle  $\phi$  will not affect the resulting waveform [56]. Second, because  $h_{+, \times}$  is real, we must include the terms  $\pm m$  ( $|m| \leq \ell$ )

when carrying out the summation in Eq. (34). We will consider  $\ell = 2$  only and assume that the amplitudes  $A_{2m}$  are as follows:

$$A_{22} = A_{2,-2} = 1, \quad \text{and} \quad A_{21} = A_{2,-1} = A_{20} = 0. \quad (36)$$

Together with spherical symmetry, they imply that

$$X_{22}^{(\pm)} = X_{2,-2}^{(\pm)} \equiv X_2^{(\pm)} \quad (37)$$

are the only nonzero contributions to Eq. (34). Having made this many assumptions, we do not shy away from making a third one: to simplify the forthcoming analysis we will study only one polarization at a time, which we choose to be  $h_+$  for the most part of our discussion.

Under these assumptions, Eq. (34a) reduces to:

$$r h_+ = f^{(+)}(\theta, \phi) X_2^{(+)} + f^{(-)}(\theta, \phi) X_2^{(-)}, \quad (38)$$

where we defined

$$f^{(+)} = \frac{1}{4} \sqrt{\frac{15}{2\pi}} [3 + \cos 2\theta] \cos 2\phi, \quad (39a)$$

$$f^{(-)} = \sqrt{\frac{30}{\pi}} \cos \theta \sin \phi \cos \phi, \quad (39b)$$

and  $r$  is a location far from the black hole that we take to be the extraction radius  $r_{\text{ext}}$ . We notice that once we fix the angles  $\theta$  and  $\phi$ , the “form factors”  $f^{(\pm)}$  are degenerate with the amplitude  $A_{\ell m}$  of our initial data (19). Moreover,  $h_+$  is completely determined by the parity-even contribution if  $\theta = \pi/2$  or when  $\phi = 0, \pi/2, \pi, 3\pi/2$ , or  $2\pi$ . Conversely,  $h_+$  is completely determined by the parity-odd contribution if  $\phi = \pi/4$  or  $3\pi/4$ .

To analyze how isospectrality breaking affects  $h_+$ , we choose  $\varepsilon = 0.05$  and study three pairs of angles  $(\theta, \phi)$  as summarized next:

1. *Comparable mixing:* we set  $(\theta, \phi) = (\pi/3, \pi/6)$ . For these angles,  $f^{(+)} \approx f^{(-)} \approx 0.67$ . Thus, axial and polar waveforms  $X^{(\pm)}$  have comparable contributions to  $h_+$ .
2. *Polar dominated:* we set  $(\theta, \phi) = (2\pi/5, \pi/10)$ . For these angles,  $f^{(+)} \approx 1.03$  and  $f^{(-)} \approx 0.28$ . Thus, the polar waveform  $X^{(+)}$  is the dominant contribution to  $h_+$ .
3. *Axial dominated:* we set  $(\theta, \phi) = (\pi, \pi/3)$ . For these angles,  $f^{(+)} \approx -0.39$  and  $f^{(-)} \approx -1.34$ . Thus, the axial waveform  $X^{(-)}$  is the dominant contribution to  $h_+$ .

In Fig. 14, we show the resulting waveforms for each of these cases. All waveforms are shifted in time such that their peaks occur at  $t = t_{\text{peak}}$ . Moving left to right, the columns show the comparable-mixing, polar-dominated, and axial-dominated cases. In the top row, we compare the gravitational-wave polarization  $h_+$  in the EFT with  $\varepsilon = 0.05$  (solid line) against general relativity  $\varepsilon = 0$  (dashed line). For each column, we show in the bottom row  $h_+$  (again, for  $\varepsilon = 0.05$ , solid line) versus the polar [(+), dot-dashed line], and axial [(-), dashed line] master-function waveforms. The latter two were multiplied by the respective form-factors  $f^{(\pm)}$ .

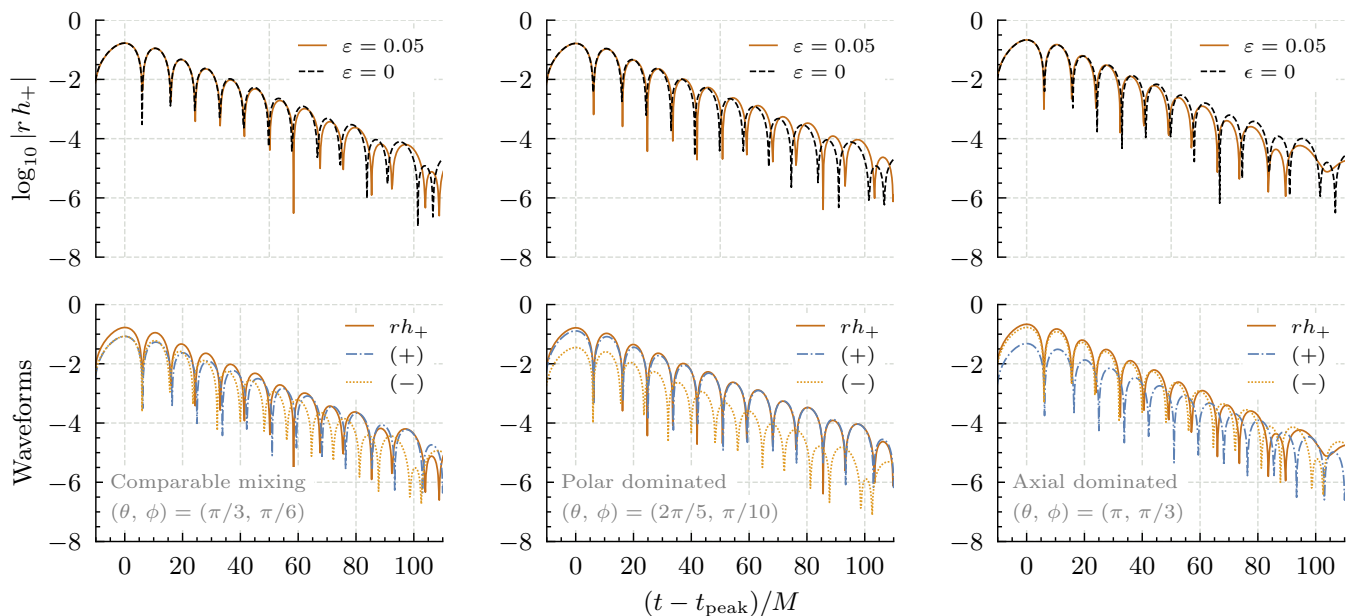


FIG. 14. Gravitational waveforms. From left to right, we show the comparable-mixing, polar-dominated, and axial-dominated cases, respectively. In the top row, we compare  $rh_+$  in the EFT with  $\varepsilon = 0.05$  (solid line) and general relativity  $\varepsilon = 0$  (dashed line). In the bottom row, we compare  $rh_+$  (for  $\varepsilon = 0.05$ , solid line) versus the polar [(+), dot-dashed line] and axial [(-), dashed line] master-function waveforms. We shifted all waveform in time such that their peaks occur at  $t = t_{\text{peak}}$ .

A common trend can be seen in the panels in the bottom row. Let us start with the comparable-mixing case shown in the leftmost bottom panel. As expected, we see that at the start of the ringdown both axial and polar waveforms contribute equally to  $h_+$ . However, as time progresses,  $h_+$  becomes more similar to the polar waveform  $X^{(+)}$ ; compare  $h_+$  and  $X^{(+)}$  in the intervals  $0 \lesssim t/M \lesssim 50$  and  $50 \lesssim t/M \lesssim 100$  after the peak of the waveform  $t_{\text{peak}}$ . This happens because the axial fundamental quasinormal frequency  $\omega_{20}^{(-)}$  has a smaller imaginary part than its polar counterpart; see Eq. (32). For this reason,  $X^{(-)}$  decays faster in time, eventually leaving  $X^{(+)}$  as the dominant contribution to ringdown. This effect is also visible in the polar-dominated case shown in the middle bottom panel. We see that the small difference between  $h_+$  and  $X^{(+)}$  at  $t = t_{\text{peak}}$  decreases as the ringdown progresses, and the two curves become virtually identical approximately  $50M$  after  $t_{\text{peak}}$ . The opposite behavior happens in the axial-dominated case shown in the rightmost bottom panel. In this case,  $h_+$  and  $X^{(-)}$  are very similar to one another at the beginning of the ringdown, and differences between the two become visible at  $50M$  after  $t_{\text{peak}}$ .

What about the comparison against general relativity? In the comparable-mixing case (leftmost top panel),  $h_+$  is virtually indistinguishable initially in the EFT and in general relativity. Differences between the two waveforms only become visible at about  $50M$  after  $t_{\text{peak}}$ . We interpret this result as follows. Early in the ringdown, the polar and axial fundamental quasinormal frequencies

combine into an “effective frequency”

$$M\omega_{20}^{\text{eff}} = \frac{M}{2} \left[ \omega_{20}^{(+)} + \omega_{20}^{(-)} \right] \approx 0.376639 - 0.0876343i, \quad (40)$$

which is approximately equal to the Schwarzschild fundamental quasinormal frequency (29). The axial mode decays faster in time as discussed previously, causing  $\omega_{20}^{\text{eff}} \approx \omega_{20}^{(+)}$  as time progresses. Indeed, the differences between the two waveforms become apparent  $50M$  after  $t_{\text{peak}}$ . In the polar- and axial-dominated situations (middle and right panels in the top row, respectively) the EFT corrections are, to some extent, visible earlier in the ringdown, as expected.

### C. Quasinormal frequency extraction

Having constructed the waveforms  $h_+$ , we now explore to what extent we can extract the *two fundamental quasinormal frequencies* that are predicted by EFT.

#### 1. Theory-agnostic single-frequency fits

We begin by considering the same theory-agnostic single-frequency fit we applied to  $X^{(\pm)}$  in Sec. IV B 3, but now we applied to  $h_+$ . As a sanity check, we first used this fit to the comparable-mixing case, but in general relativity. Unsurprisingly, we were able to recover the fundamental Schwarzschild quasinormal frequency (29) to within 1% for  $t_0 \geq 10M$ . Our results are very similar to those shown in Figs. 11 and 12.

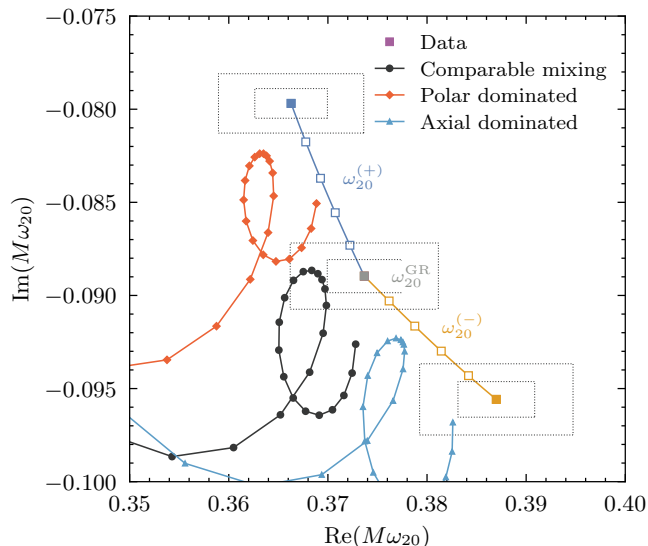


FIG. 15. Trajectories in the complex plane for the best-fit fundamental quasinormal frequencies  $\omega_{20}$  recovered from  $h_+$ , as  $t_0$  varies from zero to  $30M$ . As in Fig. 11, the squares indicate quasinormal frequencies in general relativity and in the effective field theory. The dotted-lined rectangles represent  $\pm 1\%$  and  $\pm 2\%$  away from reference value of  $\omega_{20}$  when  $\varepsilon = 0$  [Eq. (29)] and  $\varepsilon = 0.05$  [Eq. (32)]. The trajectories show that we are unable to accurately recover either of two fundamental quasinormal frequencies present in  $h_+$ , strikingly, even in the polar and axial dominated cases.

We then applied the same fitting procedure but now for  $\varepsilon = 0.05$  and the three cases enumerated in Sec. VB. The results are summarized in Fig. 15. Similarly to Fig. 11, we show the trajectories in the complex plane for the best fit quasinormal frequencies  $\omega_{20}$  recovered from  $h_+$  as we varied the start of the fit time-window  $t_0$  from zero to  $30M$ . We were unable to recover either of the fundamental quasinormal frequencies (32) in the three cases. In the polar and axial-dominated cases, the curves whirl toward the region in the complex plane where the polar and axial quasinormal frequencies move away from their general-relativistic values as  $\varepsilon$  increases. While the two trajectories do seem to converge, they do so at none of the frequencies of the black hole. Our best-fit frequencies are thus biased. Because *we were* able to recover the fundamental quasinormal frequencies when we analyzed the individual  $X^{(\pm)}$  functions, we conclude that the *mixing of frequencies in  $h_+$  is the cause of this result*. Interestingly, we see that the trajectory for the comparable-mixing case whirls toward the Schwarzschild quasinormal frequency, being 2% away from this frequency for  $13 \lesssim t_0/M \lesssim 19$ . This observation supports our interpretation from Sec. VB that at least during some time in the ringdown the two EFT fundamental quasinormal frequencies behave as a single effective frequency (40) that, in the EFT, has a numerical value close to the general-relativity value (29).

The deterioration of our ability to recover the frequencies in the polar and axial dominated cases is qualitative

similar to the conclusions of Ref. [57].

We also experimented using a two-frequency fit to analyze  $h_+$ , with the hope that we could accurately extract either of the two fundamental quasinormal frequencies from the waveform. We used Eq. (27) with  $N = 1$ , increasing the number of free parameters in our model from four to eight. We attempted to fit all parameters simultaneously. The result was disastrous: neither frequencies converged as we varied the time-window parameter  $t_0$ .

In light of these sobering results, we turn to a (perhaps) more modest question: can we infer the presence of a nonzero value of  $\varepsilon$ ?

## 2. Can we infer a nonzero $\varepsilon$ ?

After having performed theory-agnostic fits for the waveform  $h_+$ , we now discuss an EFT-informed fit. This means that the complex frequency of the fundamental mode is not left free to vary but is assumed to take the form predicted by our EFT:  $\omega_{\ell n}^{(\pm)} = \omega_{\ell n}^{\text{GR}} + \varepsilon \delta\omega_{\ell n}^{(\pm)}$ . For the case of  $\ell = 2$  and  $n = 0$ , the linear correction to the frequencies can be evaluated to be

$$M\delta\omega_{20}^{(+)} = -0.145410 + 0.166074i, \quad (41a)$$

$$M\delta\omega_{20}^{(-)} = +0.250595 - 0.133418i. \quad (41b)$$

In order to avoid confusion, we refer to  $\omega^{(+)}$  in Eq. (41a) as the *even* mode and to  $\omega^{(-)}$  in Eq. (41b) as the *odd* mode. These frequencies correspond, respectively, to the polar and axial quasinormal-frequencies. Notice that the even mode is longer-lived compared to the odd mode.

With this procedure, we can test whether the two parities contained in the waveform can be extracted, so to improve the two-frequencies fit. As we will see, even with this procedure, the extraction of the two modes remains difficult. On the other hand, we will show that, for configurations dominated by a single parity mode, our fits give a preference for the correct parity. However, for EFT waveforms, the best-fit value for the EFT parameter  $\varepsilon$  does not always align with the correct value. Below we will discuss the results of our fits, obtained by following the same procedure as in Sec. IV B 3. In the least-square fitting, we utilize the same bounds for the amplitude and phase, while imposing the following bound on the EFT parameter  $\varepsilon \in [0, 0.2]$ .<sup>3</sup>

First, we consider a waveform in general relativity with comparable polar and axial components, i.e., the “comparable mixing” case of Sec. VB. We then perform a single-mode fit, first with a “even-mode” assumption for the frequency (41a) and then with an “odd-mode” assumption (41b). We show the results for the two fits in

<sup>3</sup> To avoid too stringent priors on  $\varepsilon$ , we chose the upper limit to be 0.2, which is outside of the regime where EFT corrections are linear [17]. However, we checked that changing this value does not alter our results.

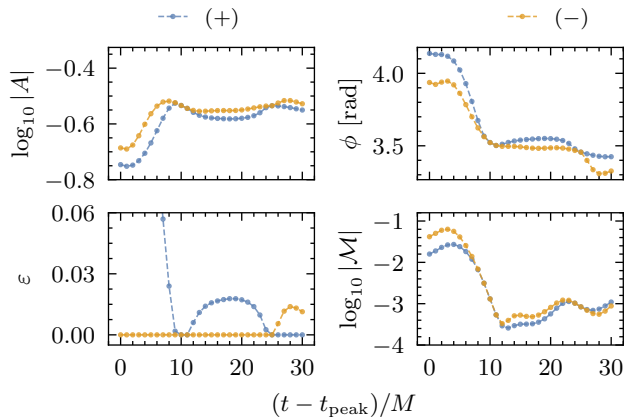


FIG. 16. Dependence of the mismatch and the best-fit parameters in our fitting model as functions of  $t_0 = t - t_{\text{peak}}$  for the waveform  $h_+$  in general relativity obtained using Eq. (38) in the comparable-mixing configuration and the master function shown in Fig. 8, assuming an EFT form for the quasinormal-mode frequencies.

Fig. 16. Both models (even and odd parametrizations of the fundamental frequency) produce similar results for the amplitude  $|A|$ , phase  $\phi$  and mismatch  $\mathcal{M}$ . Regarding  $\varepsilon$ , we notice that the odd-mode fit consistently obtains  $\varepsilon \simeq 0$ , while the even-mode fit prefers a nonvanishing (but small) value for this parameter. Among the two fits, the best overall fit is achieved for the even model when  $(t - t_{\text{peak}}) \simeq 12M$  and with  $\varepsilon \simeq 0.01$ . This result establishes the sensitivity of our analysis, indicating that a value of  $\varepsilon \simeq 0.01$  is the smallest deviation from general relativity our model can confidently distinguish from zero.

As a second test, we consider an EFT waveform with  $\varepsilon = 0.05$  in two configurations: the *polar* and *axial dominated* cases of VB. In the two angular configurations, we fit the waveform  $h_+$  with both even (41a) and odd-mode (41b) models. For simplicity, for each angular configuration, we keep the best fit between even- and odd-mode models. The goal in these cases is to find a preference for the correct parity and recover the correct value for  $\varepsilon$ .

We show our results for the polar and axial-dominated configurations in the top and bottom set of panels in Fig. 17, as indicated therein. For the polar-dominated configuration, we obtain the smallest mismatch when starting the fit around  $(t - t_{\text{peak}}) \simeq 12M$  after the peak. The best fitting model is, as expected, the even-mode model. Moreover, the recovered value for  $\varepsilon$  (best fit) is approximately 0.049, very close to the true value, 0.05, indicated by the dashed horizontal line. For the axial-dominated configuration, the smallest mismatch is again obtained starting approximately at  $12M$  after the peak, with the odd-mode model correctly identified. Contrary to the polar-dominated configuration, the recovered value for  $\varepsilon$ , around 0.022, is not as precise.

Let us comment on the results of the fits in these two angular configurations. First, the fitting procedure provides stable results. Indeed, in all cases, within the

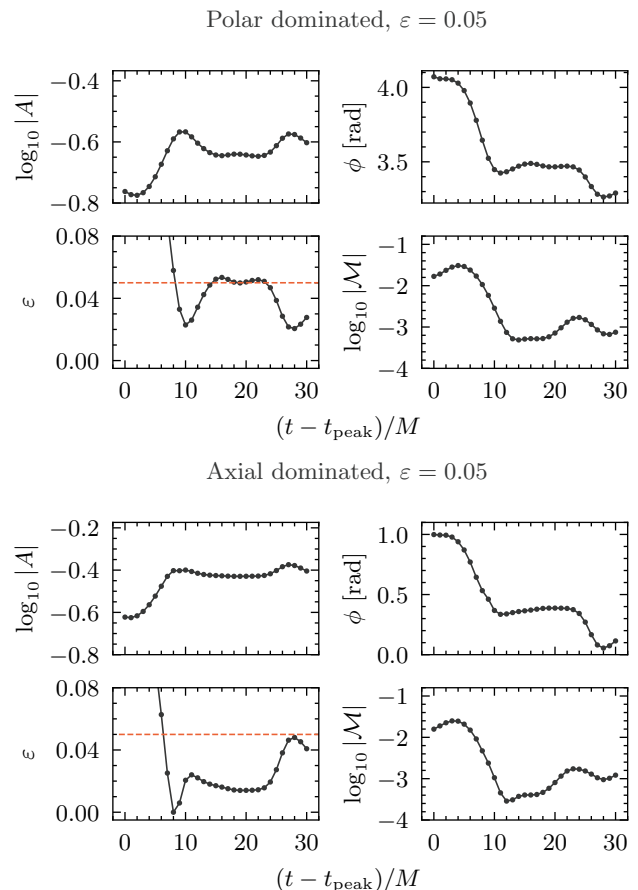


FIG. 17. Dependence of the mismatch and the best-fit parameters in our fitting model as functions of  $t_0 = t - t_{\text{peak}}$  for the EFT waveform  $h_+$  obtained using Eq. (38) in the polar-dominated (top set of panels) and axial-dominated (bottom set of panels) configurations. We set  $\varepsilon = 0.05$  in both cases; this value is indicated by the horizontal dashed line in the lower-left panels. In each case, the smallest mismatches are obtained when we use the even (odd) ansatz for the quasinormal frequency (41) to analyze the polar dominated (axial dominated) configuration, as expected.

time window between 10 to  $20M$  after the peak, the fits return constant values for the parameters. In this region, the mismatch is also minimized. Second, the polar-dominated configuration provides a better reconstruction for  $\varepsilon$ . This result can be understood by recalling that, in the EFT, the polar mode is longer-lived than the axial mode. This means that it is easier to fit for the polar mode, as it contributes more at later times. On the other hand, the axial mode decreases more quickly and is thus less “visible.”

In addition to the two fits above, we have also tested the EFT-informed fit in the “comparable mixing” configuration, where both parities are similarly excited, with  $\varepsilon = 0.05$ . Here, the fits slightly prefer the even-mode model, with a poorly reconstructed value of  $\varepsilon \simeq 0.01$ . Given the general poor reconstruction for  $\varepsilon$ , we did not attempt to perform an EFT-informed two-mode fit, i.e., fit-

ting simultaneously for two amplitudes and phases and  $\varepsilon$ , assuming the two frequencies follow Eqs. (41a) and (41b).

As an additional test for our fits, we have repeated them with  $h_{\times}$  instead of  $h_{+}$ . The former waveform is obtained using Eq. (34b) (also in this case, we consider  $\ell = 2$  and the sum over  $m = \pm 2$ ). From this formula, we notice that, compared to  $h_{+}$ , the roles of  $X_{\ell m}^{(+)}$  and  $X_{\ell m}^{(-)}$  are switched, and the overall sign is flipped. This means in particular that a polar-dominated angular configuration for  $h_{+}$  corresponds to an axial-dominated configuration for  $h_{\times}$ . We then find consistent results with the previous analysis: in polar-dominated configurations for  $h_{\times}$ , we are able to recover the parameter  $\varepsilon$  accurately and identify the correct mode, while in axial-dominated configurations,  $\varepsilon$  is poorly reconstructed, but the mode is identified correctly.

Finally, we end by commenting on the case where  $\varepsilon$  is not imposed to be positive, but allowed to take any sign. In this case, we find that the fits generically degrade, and in particular, polar (axial) dominated configurations can be fitted better by the odd (even) model. This can be understood by noticing the presence of an approximate degeneracy when sending  $\varepsilon \rightarrow -\varepsilon$  and by exchanging the mode parity. Indeed, by inspecting Fig. 11, one sees that by continuing the straight trajectory for, say,  $\omega^{(+)}$  to negative  $\varepsilon$ , we remain close to the  $\omega^{(-)}$  trajectory with  $\varepsilon > 0$ . Therefore, fitting the waveform with  $\omega^{(+)}$  and  $\varepsilon < 0$  yields similar mismatches as with  $\omega^{(-)}$  and  $\varepsilon > 0$ . This further highlights the difficulty in correctly identifying deviations from general relativity, and in particular, isospectrality breaking, in realistic ringdown data.

## VI. CONCLUSIONS AND OUTLOOK

We presented a first study of how isospectrality breaking affects the time-domain gravitational-wave polarizations in the ringdown of perturbed nonrotating black holes in an EFT extension of general relativity. We began by evolving in time the master equations that dictate the dynamics of polar and axial perturbations using momentarily static Gaussian initial data. We then proposed a prescription on how to combine the resulting polar and axial-perturbation waveforms to construct the complete gravitational waveform. With these waveforms in hand, we explored to what extent we can distinguish the presence of the two fundamental quasinormal frequencies in the signal, the chief implication of the loss of isospectrality.

Our main conclusions are clear. First, it is hard to infer the presence of these two modes when using a model agnostic fit for the ringdown. The presence of a doublet of fundamental quasinormal frequencies in the signal deteriorates our ability to recover either. Second, using a ‘‘EFT-informed’’ model (in which the damping and oscillation frequency of the quasinormal modes are written as a perturbative expansion in the EFT parameter  $\varepsilon$  around their Schwarzschild values), however, we were at least able to infer the presence of a deviation of general relativity in the signal. Still, this is only possible when the ringdown

is dominated by the polar fundamental mode, which has the slowest damping time from the doublet.

We entertain the possibility that similar conclusions will be shared in the ringdown of nonrotating black holes in other theories that are perturbatively close to general relativity and possess only massless degrees of freedom. Examples include EFTs of general relativity with quartic-in-curvature terms and theories that involve nonminimal coupling of (pseudo)scalar fields with curvature scalars, such as shift-symmetric Einstein-scalar-Gauss-Bonnet and dynamical Chern-Simons gravity.

How do our conclusions depend on our assumptions? First, while the relation (34) between  $h_{+, \times}$  and the ZM (polar) and CPM (axial) master functions hold in the EFT, there is clearly room to improve how the latter were computed. As discussed in Sec. VB, a self-consistent calculation of the gravitational waveforms can be made using a test particle, whose geodesic motion excites the black-hole perturbations. This problem will be tackled in an upcoming paper in this series [55]. Still, it is tempting to conjecture that our main conclusions will be shared in such a calculation. This is justified by the flexibility of our construction leading to Eq. (38) in accommodating the relative contributions of the axial and polar contributions to the waveform. Second, we have considered only nonrotating black holes. Quasinormal frequency calculations of rotating black holes in the EFT considered herein show that the fundamental polar and axial quasinormal frequencies can deviate more from their general-relativity values for larger black hole spins [58, 59]. It would be important to understand how rotation affects our findings.

In summary, there is much to be done yet to understand the quasinormal modes, their excitation, and observational implications in theories beyond general relativity.

## ACKNOWLEDGEMENTS

We thank Barry Wardell for the suggestion of carrying out scattering experiments to study the loss of quasinormal mode isospectrality in our problem and Helvi Witek for numerous discussions and advice. We thank Mark Ho-Yeuk Cheung for correspondence and sharing with us data from Ref. [48] which we used to validate our fitting routines. We also acknowledge discussions with Jamie Bamber, Caio F. B. Macedo, Jan Steinhoff, Antonios Tsokaros, Sebastian Völkel, and Daiki Watarai. Some of our calculations were done with the MATHEMATICA packages xPERT [60] and INVAR [61, 62], parts of the xACT/xTENSOR suite [63, 64]. H.O.S. acknowledges funding from the Deutsche Forschungsgemeinschaft (DFG) - Project No.: 386119226. K.Y. acknowledges support from NSF Grant PHY-2309066 and PHYS-2339969.

## Appendix A: Code details and validation

In this appendix, we provide details of our numerical code and describe the convergence tests we performed to validate it. We evolved Eq. (22) using the method of lines. In particular, our code uses fourth order accurate-in-space finite difference stencils and evolve the variables  $X$ ,  $\Psi$ , and  $\Pi$  forward in time using the third-order accurate Runge–Kutta scheme of Shu and Osher [40]. We also implemented, and tested, a fourth-order accurate Runge–Kutta scheme. We opted to use the third-order scheme as a compromise between accuracy and simulation run times. The code is written in C++ and uses OpenMP for parallelization.

### 1. Grid size and boundary conditions

In all our simulations we used a uniform spatial grid ranging from  $r_*^{\min} = -30M$  to  $r_*^{\max} = 600M$ , while time integration was carried out from  $t = 0$  to  $t = 720M$ . Our choices for the grid parameters require some justification. Let us begin with the spatial domain. Because we employ tortoise coordinates in our spatial grid, we must compute numerically the inverse relation

$$r = r(r_*; \varepsilon), \quad (\text{A1})$$

to evaluate the propagation speed and effective potential in Eq. (10). The explicit expression for  $r_* = r_*(r; \varepsilon)$  can be found in Ref. [17], Appendix D.

In general relativity,  $\varepsilon = 0$ , the two coordinates are related as follows:

$$r_* = r + 2M \ln |r/(2M) - 1|. \quad (\text{A2})$$

Equation (A2) can be inverted using the Lambert  $W$  function [65, 66]. This function is defined as the solution to the equation

$$W(z) e^{W(z)} = z. \quad (\text{A3})$$

In our problem, we find that

$$r = 2M [1 + W(z)], \quad z = \exp[r_*/(2M) - 1]. \quad (\text{A4})$$

The function  $W(z)$  has two real values in the interval  $-1/e \leq z < 0$ ; see Fig. 18 for an illustration. In particular, at  $z = -1/e$ ,  $W(z) = -1$ . The principal branch of the Lambert  $W$  function is defined by  $-1 \leq W(z)$ . In our case  $z \in [0, \infty)$ , and this is the branch we must use.

When  $\varepsilon \neq 0$ , we calculate (A1) numerically by locating the root of  $\varrho(r_*; \varepsilon) = r - r(r_*; \varepsilon)$ . To do this, we first compute a value of  $r$  using the general relativistic result (A4). Call it  $r_0 = r(r_*; 0)$ . We then calculate  $r_L = r_0(1 - \delta r)$  and  $r_R = r_0(1 + \delta r)$  that serve as educated guesses to bracket the root, which we determine through bisection. We found that  $\delta r = 0.1$  works for this task for all values of  $\varepsilon$  considered in this paper. When computing  $r_L$  we must

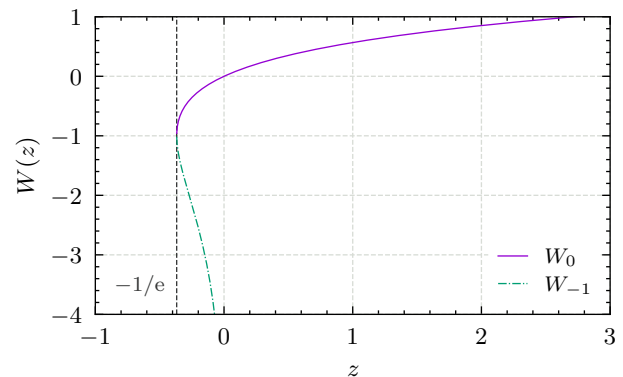


FIG. 18. The two real branches of the Lambert  $W$  functions,  $W_0$  (solid line) and  $W_{-1}$  (dot-dashed line). The principal branch  $W_0$  is defined by  $-1 \leq W$ , this occurs for  $-1/e \leq z$  (dashed gray line).

ensure that it is not located inside the event horizon,  $r_h$ . To avoid this edge case, we first check if  $r_L \geq r_h$ . If this is true, we use the foregoing expression for  $r_L$ . If false, we set  $r_L = r_h(1 + 10^{-10})$ . In practice, our code uses the implementations for the Lambert  $W$  function and bisection algorithm from the Boost C++ libraries [67].

When setting up the numerical grid in  $r_*$ , we must be careful with the fact that  $r/r_h$  is indistinguishable from 1 at double precision for any  $r_*/r_h \lesssim -30$  when  $\varepsilon = 0$ , for which  $r_h = 2M$ . In other words, the tortoise coordinate  $r(r_*)/r_h$  will evaluate exactly to 1 for any value of  $r_*/r_h$  smaller than approximately  $-30$ . For this reason, we restrict ourselves to  $r_*^{\min}/r_h > -30$ . In general relativity, this translates into  $r(r_*^{\min})/r_h - 1 \gtrsim 3.5 \cdot 10^{-14}$ , which gives us a rule of thumb of how slightly outside the event horizon our numerical grid can begin. In practice, we choose  $r_*^{\min} = -30M$ . The reason is twofold. First, it satisfies the above bound. Second, for this value, both  $c_s^2$  and  $V_\ell^{(\pm)}$  are sufficiently close to zero for us to impose outgoing boundary conditions at the edge of our numerical grid as if we had a simple one-dimensional wave equation propagating with constant velocity. This partly justifies our choice of  $r_*^{\max} = 600M$  too. The remaining justification, and the explanation of our choice of time integration range, is that we wish to avoid numerical reflections from the boundaries to appear in our waveforms given the parameters of the initial data. We give more details below.

### 2. Initial data and waveform extraction

We set the parameters of the Gaussian initial data (19) to be

$$A = 1, \quad \sqrt{2}\sigma = 1.5M, \quad \text{and} \quad r_*^{\text{med}} = 100M. \quad (\text{A5})$$

The width  $\sigma$  of the Gaussian is chosen to be smaller than the lengthscales associated with the spatial extension in which the propagation speed  $c_s^2$  and the effective potential

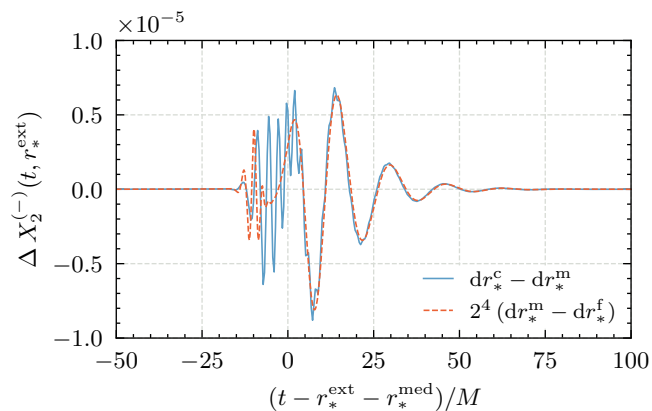


FIG. 19. Local convergence analysis of the quadrupolar CPM waveform extracted at  $r_*^{\text{ext}} = 150M$ , computed with different spatial resolutions  $dr_*$  and fixed Courant factor  $C = 0.2$ . The figure shows the difference between the waveforms obtained using coarse ( $dr_*^c = 0.2M$ ) and medium ( $dr_*^m = 0.1M$ ) resolutions (solid line) and medium and fine ( $dr_*^f = 0.05M$ ) resolutions (dashed line). We shifted the curves in time by the extraction radius  $r_*^{\text{ext}}$  and initial location of the Gaussian’s peak,  $r_*^{\text{med}} = 100M$ . We rescaled the latter curve by the expected convergence factor,  $2^4$ . The overlap between the two curves demonstrates the fourth order convergence of the code.

$V_\ell^{(\pm)}$  are nonzero. In this way, we can observe the effects of  $c_s^2$  and  $V_\ell^{(\pm)}$  in the scattered wave.

The value of the scattered wave, that is, the waveform, is extracted at a radius  $r_*^{\text{ext}} \geq \sigma$  of  $\mathcal{O}(10^2 M)$ . For these values of  $r_*^{\text{ext}}$ ,  $\sigma$ , and  $r_*^{\text{min}/\text{max}}$ , we avoid the contamination in our waveforms from numerical noise of small amplitude originating from reflected waves at the boundaries of the spatial grid in the duration of our simulations.

### 3. Convergence tests and error estimates

In Fig. 19, we show the results of our local convergence test. We chose a Courant factor  $C = dt/dr_* = 0.2$ .<sup>4</sup> We then performed three simulations with increasing spatial resolution,  $dr_* = \{0.05, 0.1, 0.2\}$ , with fixed values of the effective-field-theory parameter  $\varepsilon = 5 \times 10^{-2}$ , considering the Regge–Wheeler potential  $V_\ell^{(-)}$ , and quadrupolar  $\ell = 2$  perturbations. The waveform was extracted at  $r_*^{\text{ext}} = 100M$ . The solid and dashed curves show the difference between the waveforms produced in the coarse ( $dr_*^c = 0.2M$ ) and medium ( $dr_*^m = 0.1M$ ) and medium and fine ( $dr_*^f = 0.05M$ ) resolutions, respectively. We rescaled the

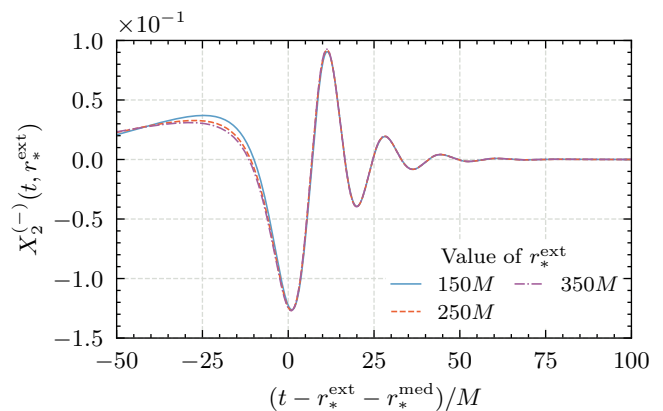


FIG. 20. Quadrupolar CPM waveform extracted at three different radii  $r_*^{\text{ext}} = 150M$  (solid line),  $250M$  (dashed line), and  $350M$  (dot-dashed line). We use a spatial grid resolution of  $dr_* = 0.1M$  and a Courant factor  $C = 0.2$ , i.e., the medium resolution setup in Fig. 19. The waveforms are shifted in time according to where they were extracted,  $r_*^{\text{ext}}$  and initial location of the Gaussian’s peak,  $r_*^{\text{med}} = 100M$ . The overlap between the waveforms demonstrates that numerical dispersion and dissipation are small in the code.

latter curve by  $2^4$ , the expected convergence factor in our test. The resulting overlap between the two curves demonstrates the fourth-order convergence of the code. All the simulations presented in the main text use the medium spatial resolution and Courant factor  $C = 0.2$ .

To tell apart the effects of the effective-field-theory parameter  $\varepsilon$  from numerical noise, it is important to quantify the error associated with our waveforms. Because our code is in the convergence regime (as shown in Fig. 19), we calculated the absolute value of the difference between our coarse- and medium-resolution waveforms and divided by  $2^4 - 1$  [68]. Taking the absolute value and then the mean value of this quantity, we arrive at the error estimate of  $\mathcal{O}(10^{-6})$  in our waveforms. This is smaller than the values of  $\varepsilon$  we consider that are  $\mathcal{O}(10^{-2})$ . Consequently, we can interpret the changes in the waveforms produced by varying values of  $\varepsilon$ , while keeping the other simulation parameters fixed, as originating from the higher-curvature corrections instead of numerical errors.

We also performed another check of our code. Figure 20 shows the quadrupolar Regge–Wheeler waveform from the medium resolution simulation of our local convergence test, with the waveform extracted at three different radii,  $r_*^{\text{ext}} = 150M$  (solid line),  $250M$  (dashed line), and  $350M$  (dot-dashed line). Each waveform is shifted in time according to its extraction radius,  $r_*^{\text{ext}}$ , and initial location of the Gaussian’s peak,  $r_*^{\text{med}}$ . We see that the three waveforms overlap, notably in the ringdown. This demonstrates that numerical dissipation and dispersion are small in the code. However, there is a small difference between the waveforms in the (approximate) interval  $(t - r_*^{\text{ext}} - r_*^{\text{med}})/M \in [-50, 0]$ . We attribute this difference to the proximity of the smallest extraction radius to the initial data. Indeed, we see that the difference

<sup>4</sup> Because the propagation speed  $c_s$  has spatial dependence, using the same Courant factor  $C$  across the numerical domain may not be appropriate. That is, we should be careful and include some information about  $c_s$ , for instance, its maximum value, when choosing the Courant factor. However, this is not an issue in our problem because we choose a small value of  $C$ , and  $c_s^2$  deviates from unity by at most by 3%; see Fig. 2.

between the waveforms decreases as  $r_*^{\text{ext}}$  increases.

## Appendix B: The wave equation with a position-dependent propagation speed

### 1. Change of variable to $c_s = 1$

The evolution equation with a position-dependent speed of sound  $c_s(x)$  can be mapped into an equation with  $c_s = 1$  and a modified potential; see Eq. (24) in the main text. In this appendix, we follow the presentation in Ref. [47] and re-derive the transformed equation. We start with the following frequency-domain equation

$$\psi''(x) + \frac{\omega^2}{c_s^2(x)}\psi(x) - V(x)\psi(x) = 0. \quad (\text{B1})$$

To achieve our goal, we change variable from  $x$  to  $y$  and introduce a new field:

$$\varphi(y) = \psi(x(y))/\sqrt{\dot{x}(y)}, \quad (\text{B2})$$

where the overdot stands for the derivative with respect to  $y$  (not to be confused with a time derivative). Let us call  $g(y) = \sqrt{\dot{x}}$ . Then, we find that

$$g' = \frac{1}{2g} \frac{\ddot{x}}{\dot{x}}, \quad (\text{B3a})$$

$$g'' = \frac{1}{g^3} \left[ \frac{1}{2} \frac{d}{dy} \left( \frac{\ddot{x}}{\dot{x}} \right) - \frac{1}{4} \left( \frac{\ddot{x}}{\dot{x}} \right)^2 \right] \equiv \frac{1}{g^3} \{x, y\}, \quad (\text{B3b})$$

$$\varphi' = \frac{\dot{\varphi}}{g^2}, \quad (\text{B3c})$$

$$\varphi'' = \frac{1}{g^4} \left[ \ddot{\varphi} - \frac{\ddot{x}}{\dot{x}} \dot{\varphi} \right]. \quad (\text{B3d})$$

In Eq. (B3b) we identified the Schwarzian derivative:

$$\{x, y\} = \frac{1}{2} \frac{d}{dy} \left( \frac{\ddot{x}}{\dot{x}} \right) - \frac{1}{4} \left( \frac{\ddot{x}}{\dot{x}} \right)^2. \quad (\text{B4})$$

Using these expressions in Eq. (B1) we obtain

$$\ddot{\varphi} + \left[ g^4 \left( \frac{\omega^2}{c_s^2(x(y))} - V(x(y)) \right) + \{x, y\} \right] \varphi = 0. \quad (\text{B5})$$

Notice that by choosing  $g^4(y) = \dot{x}^2 = c_s^2(x(y))$ , we are effectively setting  $c_s = 1$  for the field  $\varphi$ . This choice implies that

$$y(x) = \int^x dx'/c_s(x'). \quad (\text{B6})$$

With this choice, we finally obtain

$$\ddot{\varphi} + [\omega^2 - W(y)] \varphi = 0, \quad (\text{B7})$$

with the new potential

$$W(y) = c_s^2(x(y)) V(x(y)) - \{x, y\}. \quad (\text{B8})$$

The Schwarzian derivative  $\{x, y\}$  in terms of the function  $c_s(x)$  takes the form

$$\{x, y\} = \frac{1}{2} c_s c_s'' - \frac{1}{4} (c_s')^2. \quad (\text{B9})$$

Equation (B7) can be Fourier-transformed back to the time domain, resulting in a wave equation with uniform propagation speed and potential  $W$ . In the next section, we apply this procedure to the wave equation that occurs in our problem, Eq. (10).

### 2. The metric-perturbation case

The procedure outlined above can be applied to the case of the metric perturbation equations (10). These equations indeed match Eq. (B1) when identifying  $x$  with the tortoise coordinate  $r_*$ . Also, the metric perturbations  $X_\ell^{(\pm)}$  correspond to  $\psi$  and, by analogy, we define  $Y_\ell^{(\pm)}$  as the field variables after the transformation. Then, after the transformation, both axial and polar potentials  $V_\ell^{(\pm)}$  get mapped into new potentials

$$W_\ell^{(\pm)} = c_s^2(r_*(\tilde{r})) V_\ell^{(\pm)} - \{r_*, \tilde{r}\}, \quad (\text{B10})$$

where we identify  $\tilde{r}$  with  $y$ . Note that the Schwarzian and the propagation-speed rescaling affect the two original potentials in the same way, with no  $\ell$  dependence.<sup>5</sup> When formulating the equations in terms of  $Y_\ell^{(\pm)}$ , the effect of the speed of sound  $c_s$  can be quantified by evaluating the relative contribution of the Schwarzian to the potential  $W_\ell^{(\pm)}$ . In particular, we are interested in comparing this contribution with the EFT corrections already present in the potential  $V_\ell^{(\pm)}$ , given in Eq. (17).

We start with the definition of the new coordinate  $\tilde{r}$ , assigning  $x = r_*$ :

$$\tilde{r}(r_*) = \int^{r_*} dr'_* \frac{1}{c_s(r'_*)}. \quad (\text{B11})$$

For the purpose of the code implementation, it is useful to write  $\tilde{r} = \tilde{r}(r)$ . We first perform a change of variables in the integral:

$$\tilde{r}(r) = \int^{r'} dr' \frac{dr'_*}{dr'} \frac{1}{c_s(r')} = \int^{r'} dr' \frac{1}{a(r') c_s(r')}. \quad (\text{B12})$$

or in differential form:

$$d\tilde{r}/dr = (a c_s)^{-1}, \quad a = Nf. \quad (\text{B13})$$

<sup>5</sup> Let us assume for the moment the Schwarzian is the only correction to the potentials of general relativity. Even though in general relativity  $V_\ell^{(\pm)}$  are isospectral, a common shift by the function  $\{r_*, \tilde{r}\}$  does not necessarily lead to isospectral potentials.

When  $c_s = 1$ , that is, when  $\varepsilon = 0$ ,  $\tilde{r}$  is nothing but the tortoise coordinate. Using the explicit forms of  $a$  and  $c_s$ , we find

$$\frac{1}{a c_s} = \left(1 - \frac{r_h}{r}\right)^{-1} \left\{ 1 + \varepsilon \left[ \frac{5M}{8r} + \frac{5M^2}{4r^2} + \frac{5M^3}{2r^3} + \frac{5M^4}{r^4} + \frac{154M^5}{r^5} \left(1 - \frac{72r_h}{77r}\right) - \frac{88M^6}{r^6} \right] \right\}. \quad (\text{B14})$$

to leading order in  $\varepsilon$ . We integrate the differential equation (B13) for  $y$ . The solution has the schematic form:

$$\tilde{r} = r + r_h \log(r/r_h - 1) + \varepsilon \delta\tilde{r}(r), \quad (\text{B15})$$

where we chose the integration constant such that  $\tilde{r}$  reduces to the familiar tortoise coordinate in Schwarzschild when  $\varepsilon = 0$ . The particular form of  $\delta\tilde{r}$  is not illuminating.

We can now compute the Schwarzian derivative  $\{r_*, \tilde{r}\}$ :

$$\begin{aligned} \{r_*, \tilde{r}\} &= \frac{1}{2} c_s c_s'' - \frac{1}{4} (c_s')^2, \\ &= \frac{1}{2} c_s \left( a^2 \frac{d^2 c_s}{dr^2} + a \frac{da}{dr} \frac{dc_s}{dr} \right) - \frac{1}{4} \left( a \frac{dc_s}{dr} \right)^2, \\ &= -\frac{2160M^5}{r^5} \frac{\varepsilon}{r^2} \left(1 - \frac{r_h}{r}\right) \left(1 - \frac{16r_h}{15r}\right) \\ &\quad \times \left(1 - \frac{3r_h}{2r}\right). \end{aligned} \quad (\text{B16})$$

Note that  $\{r_*, \tilde{r}\}$  is not positive definite, has roots at

$$r = r_h, \quad r = 16r_h/15, \quad \text{and} \quad r = 3r_h/2, \quad (\text{B17})$$

and vanishes as  $r$  approaches infinity.

To relate the variables  $Y_\ell^{(\pm)}$  and  $X_\ell^{(\pm)}$  in our problem, we start from the analogous of Eq. (B2)

$$Y_\ell^{(\pm)}(\tilde{r}) = X(r_*(\tilde{r}))/\sqrt{dr_*/d\tilde{r}}. \quad (\text{B18})$$

Notice that

$$\frac{dr_*}{d\tilde{r}} = \frac{dr_*}{dr} \frac{dr}{d\tilde{r}} = \frac{1}{a} (ac_s) = c_s, \quad (\text{B19})$$

where, recall, we defined  $a = Nf$ .

In Fig. 21, we show in the top panel the Schwarzian  $\{r_*, \tilde{r}\}$  as a function of  $r_*$ . Its shape is not affected by  $\varepsilon$ , which gives the overall scaling. In the bottom panel, we compare the Schwarzian with the  $c_s^2 V_\ell^{(\pm)}$ , which we define as  $\delta V_\ell^{(\pm)}$ , for  $\ell = 2$ . This shows that the Schwarzian is typically smaller by an order of magnitude compared to  $\delta V_\ell^{(\pm)}$ , except around points where the latter crosses zero.

As a final remark, we connect our result to the ‘‘parametrized master equation’’ of Ref. [69], which models gravitational modifications through simple power-law corrections to the potential. The master equation for  $Y_\ell^{(\pm)}$  with potential  $W_\ell^{(\pm)}$  [Eq. (B10)] fits directly into this formalism. Specifically, it matches the structure of their Eq. (A.4) [notice that the Schwarzian derivative (B16) vanishes at the horizon], which in turn ensures its equivalence to their main Eq. (1) through a rescaling of  $Y_\ell^{(\pm)}$ .

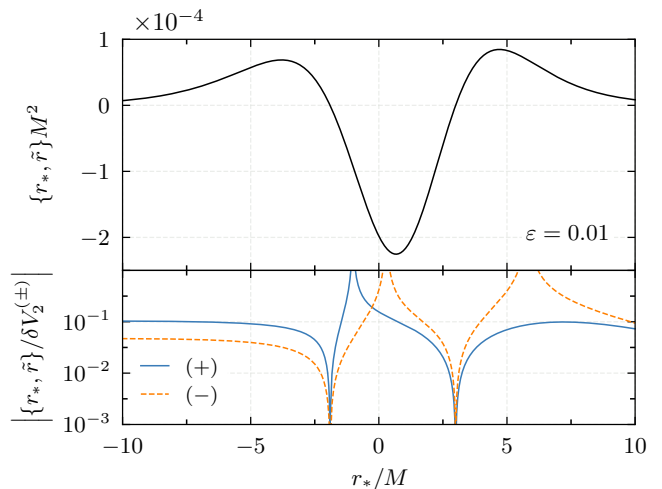


FIG. 21. The Schwarzian derivative and its comparison to the EFT corrections to the gravitational potential. Top panel: the contribution of the Schwarzian to the potential, shown in units of  $M$ , as a function of  $r_*$  for  $\varepsilon = 0.01$ . Bottom panel: The absolute value of the ratio between the Schwarzian derivative’s contribution and the EFT correction, denoted as  $\delta V_\ell^{(\pm)}$ , for the  $\ell = 2$  multipole. The blue curve represents the comparison for the polar potential (+), while the orange curve corresponds to the axial potential (-). The Schwarzian contribution is subleading compared to  $\delta V_\ell^{(\pm)}$  except when the latter function changes sign leading to singular points in the plot.

### 3. Numerical simulations

We now study the time-domain evolution of a Gaussian pulse impinging upon the ‘‘Schwarzian potential.’’ That is, we evolve Eq. (24),

$$[-\partial_{tt} + \partial_{\tilde{r}\tilde{r}} - W_\ell^{(\pm)}(r)] Y_\ell^{(\pm)}(t, r) = 0,$$

omitting the potential  $V_\ell^{(\pm)}$  in Eq. (B10), i.e.,

$$W_\ell^{(\pm)} = -\{r_*, \tilde{r}\}. \quad (\text{B20})$$

This set up is the ‘‘Schwarzian-frame’’ dual to the case (c), in which,

$$c_s^2 \neq 1, \quad \text{and} \quad V_\ell^{(\pm)} = 0, \quad (\text{B21})$$

we discussed in Sec. IV B. The initial data is similar to Eqs. (18) to (20), except that we evolve the variable  $Y_\ell^{(\pm)}$  (not  $X_\ell^{(\pm)}$ ), and we use  $\tilde{r}$  (not  $r_*$ ) for the spatial coordinate. For example, the pulse starts at  $\tilde{r}^{\text{med}} = 100M$ .

Because our initial data is momentarily static and located in a region where Eq. (B20) is negligible, the Gaussian splits symmetrically into left and right-moving parts. Figure 22 shows snapshots of the left-moving component (solid line) as it interacts with the potential (B20) (color-filled region). The dynamics unfolds similarly to what we found in Fig. 5, when the pulse entered the region where its propagation velocity is position dependent.

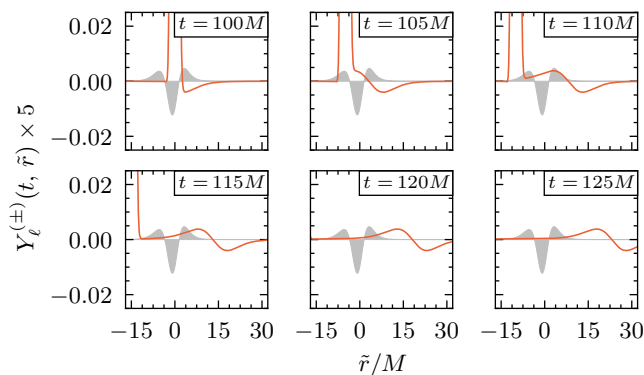


FIG. 22. Snapshots of the incident perturbation (solid line and rescaled by a factor of 5) as it impinges with constant propagation speed into the “Schwarzschild potential,” for  $\varepsilon = 0.05$ , represented by the filled gray curve. As the left-moving perturbation reaches the potential, part of it is reflected, as shown in the top panels. This reflected pulse propagates rightward (see bottom panels) and is measured by an observer at  $\tilde{r}^{\text{ext}}$  as the waveform shown in Fig. 23.

In Fig. 23, we show the waveforms

$$Y_\ell^{(\pm)}(t, \tilde{r}^{\text{ext}}) \quad \text{and} \quad X_\ell^{(\pm)}(t, r_*^{\text{ext}}), \quad (\text{B22})$$

extracted at  $\tilde{r}^{\text{ext}} = r_*^{\text{ext}} = 150M$ . Starting from  $t = 0$ , we see two pulses reaching the extraction radius. The first peak, around  $t = 50M$ , is the right-moving component reaching the extraction radius. The second peak, around  $t = 250M$ , is the part of the left-moving component that was then reflected after interacting with the region of variable propagation speed, for  $X_\ell^{(\pm)}$ , or the Schwarzschild potential, for  $Y_\ell^{(\pm)}$ . See Figs. 5 and 22, respectively. The two waveforms are similar, except for a notable difference at later times: while  $X_\ell^{(\pm)}$  decays,  $Y_\ell^{(\pm)}$  approaches an approximately constant value  $6 \times 10^{-5}$ . This value is around 5 orders of magnitudes larger than the numerical errors in our code. (Take as reference the waves reflected at the grid boundaries in the  $X_\ell^{(\pm)}$  curve around  $t \approx 350M$ .) We found that this “late-time constancy” is related to the field  $Y_\ell^{(\pm)}$  settling to a nearly constant spatial profile at the end of our simulation. This happens as long as  $\varepsilon$  is nonzero: the smaller  $\varepsilon$  is, the smaller the constant value the field settles to. We did an extensive study to understand the origin of this behavior, but ended empty handed. For this reason, we used Eq. (10) for our simulations instead Eq. (24).

It would be interesting to see if there is a relation between our results and the “anomalous permanent displacement” of the d’Alembert solution studied in Ref. [70].

### Appendix C: Dependence of the quasinormal frequency extraction on the initial data

Throughout the main text, we used a momentarily static Gaussian initial data in our simulations; see

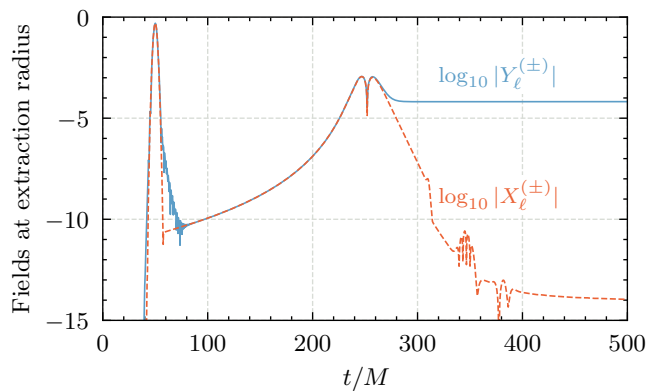


FIG. 23. The fields  $X_\ell^{(\pm)}$  (dashed line) and  $Y_\ell^{(\pm)}$  (solid line) extracted at  $\tilde{r}^{\text{ext}} = r_*^{\text{ext}} = 150M$ , for similar momentarily static Gaussian initial data centered at  $\tilde{r}^{\text{med}} = r_*^{\text{med}} = 100M$ . The initial data splits symmetrically into left and right-moving components; the latter reaches the extraction radius around  $t = 50M$ . The peaks around  $t = 250M$  are the part of the left-moving component that was reflected after interacting with the region of variable propagation speed, for  $X_\ell^{(\pm)}$ , or the Schwarzschild potential, for  $Y_\ell^{(\pm)}$ . The waveforms are similar, but at later times: while  $X_\ell^{(\pm)}$  decays,  $Y_\ell^{(\pm)}$  becomes constant.

Eqs. (18) to (20). In this appendix, we summarize the outcome of additional numerical experiments where we varied the median of the Gaussian from the value  $r_*^{\text{med}} = 100M$ , used in the main text, down to  $30M$ , while keeping the amplitude  $A = 1$  and width  $\sqrt{2}\sigma = 1.5M$  fixed. This brings the initial data from a region where it has negligible spatial overlap with the effective potential  $V_\ell^{(\pm)}$  closer to the potential’s peak; see Fig. 3.

We carried out three simulations with  $r_*^{\text{med}} = 30M$ ,  $50M$ , and  $100M$ , and then examined the waveforms’ spectral content using the method we described in Sec. IV B 3. We found that we could extract more accurately the fundamental quasinormal frequency from our time-domain data as  $r_*^{\text{med}}$  decreases. Figure 24 summarizes our results for the extraction of  $\omega_{20}$  whose numerical value in general relativity is given by Eq. (29). As in Fig. 11 we show the trajectories in the complex plane for the best-fit values of  $\omega_{20}$  as we vary the start of the fit time window  $t_0$  from zero up to  $50M$  in steps of  $1M$ . We indicate with an unfilled marker the values obtained for  $t_0 = 30M$  and  $t_0 = 50M$ . The three trajectories represent the three values of  $r_*^{\text{med}}$ , as indicated in the figure’s legend. We see that when  $r_*^{\text{med}} = 30M$ , the curve spirals closer to the true  $\omega_{20}$  value (solid square) in comparison to the  $r_*^{\text{med}} = 50M$  and  $100M$  cases. We also find that even when we extend  $t_0$  to  $50M$ , the recovered values of  $\omega_{20}$  still remain within 2% error to the true value. This does not occur in the other two cases.

In Fig. 25, we show the dependence of the best-fit parameters of our model (27) as a function of  $t_0 = t - t_{\text{peak}}$ . The vertical lines at  $t_0 = 30M$  indicate the largest value of  $t_0$  used in the main text. We see that the case  $r_*^{\text{med}} = 30M$

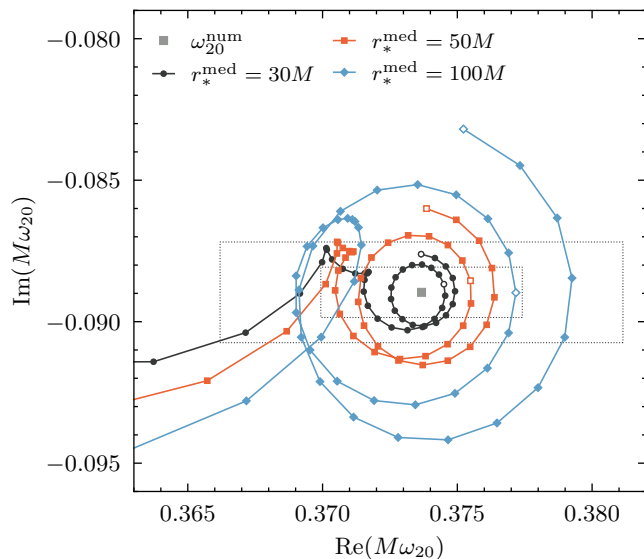


FIG. 24. Trajectories in the complex plane for the best-fit quasinormal frequencies  $\omega_{20}$  in general relativity as  $t_0 = t - t_{\text{peak}}$  varies from zero to  $30M$  (first unfilled marker following the trajectories left to right) and  $50M$  (second unfilled marker). The rectangles represent values  $\pm 1\%$  and  $\pm 2\%$  away from reference value of  $\omega_{20}$  [filled square; cf. Eq. (29).] By decreasing  $r_*^{\text{med}}$ , we can better recover  $\omega_{20}$  and also maintain less than 2% error for a wider range of values of  $t_0$ .

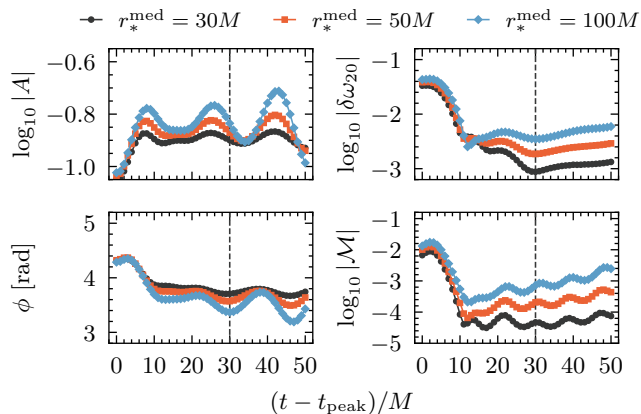


FIG. 25. Dependence of the mismatch and the best-fit parameters in our fitting model (27) as a function of  $t_0 = t - t_{\text{peak}}$ . We see the best-fit parameters are more stable when varying  $t_0$  and have smaller mismatches by making the peak of the momentarily-static Gaussian initial data,  $r_*^{\text{med}}$ , closer to the peak of the effective potential.

displays less variability in its amplitude  $A$  with respect to  $t_0$  (as long as  $t_0 \gtrsim 10M$ ) among the three cases. It is also the case that reaches the smallest absolute error,  $\delta\omega_{20}$ , has the smallest mismatch,  $\mathcal{M}$ . We were unable to identify the reason for these results. We speculate that bringing the Gaussian closer to the potential causes the quasinormal-mode amplitude of the fundamental frequency to be larger than that of its overtones. This would make the ringdown waveform become more “fundamental-mode dominated” and, consequently, our single-mode fits more accurate and stable. Our study in this appendix was done in general relativity, but we reached similar conclusions in the EFT.

[1] C. V. Vishveshwara, Scattering of Gravitational Radiation by a Schwarzschild Black-hole, *Nature* **227**, 936 (1970).  
 [2] W. H. Press, Long Wave Trains of Gravitational Waves from a Vibrating Black Hole, *Astrophys. J. Lett.* **170**, L105 (1971).  
 [3] E. W. Leaver, Spectral decomposition of the perturbation response of the Schwarzschild geometry, *Phys. Rev. D* **34**,

384 (1986).  
 [4] E. W. Leaver, An Analytic representation for the quasinormal modes of Kerr black holes, *Proc. Roy. Soc. Lond. A* **402**, 285 (1985).  
 [5] S. L. Detweiler, Black holes and gravitational waves. III. The resonant frequencies of rotating holes, *Astrophys. J.* **239**, 292 (1980).

- [6] E. Berti *et al.*, Black hole spectroscopy: from theory to experiment (2025), [arXiv:2505.23895 \[gr-qc\]](#).
- [7] T. Regge and J. A. Wheeler, Stability of a Schwarzschild singularity, *Phys. Rev.* **108**, 1063 (1957).
- [8] F. J. Zerilli, Effective potential for even-parity Regge-Wheeler gravitational perturbation equations, *Phys. Rev. Lett.* **24**, 737 (1970).
- [9] F. J. Zerilli, Gravitational field of a particle falling in a Schwarzschild geometry analyzed in tensor harmonics, *Phys. Rev. D* **2**, 2141 (1970).
- [10] S. Chandrasekhar and S. L. Detweiler, The quasi-normal modes of the Schwarzschild black hole, *Proc. Roy. Soc. Lond. A* **344**, 441 (1975).
- [11] S. Chandrasekhar, On the Potential Barriers Surrounding the Schwarzschild Black-Hole, in *Spacetime and Geometry: The Alfred Schild Lectures* (1982) pp. 120–146.
- [12] S. Chandrasekhar, On the equations governing the perturbations of the Schwarzschild black hole, *Proc. Roy. Soc. Lond. A* **343**, 289 (1975).
- [13] K. Glampedakis, A. D. Johnson, and D. Kennefick, Darboux transformation in black hole perturbation theory, *Phys. Rev. D* **96**, 024036 (2017), [arXiv:1702.06459 \[gr-qc\]](#).
- [14] N. Franchini, Slow rotation black hole perturbation theory, *Phys. Rev. D* **108**, 044079 (2023), [arXiv:2305.19313 \[gr-qc\]](#).
- [15] P. A. Cano and M. David, Isospectrality in Effective Field Theory Extensions of General Relativity, *Phys. Rev. Lett.* **134**, 191401 (2025), [arXiv:2407.12080 \[hep-th\]](#).
- [16] C. N. Pope, D. O. Rohrer, and B. F. Whiting, Perturbations of black holes in Einstein-Maxwell-dilaton-axion theories, *Phys. Rev. D* **112**, 124064 (2025), [arXiv:2508.04589 \[hep-th\]](#).
- [17] H. O. Silva, G. Tambalo, K. Glampedakis, K. Yagi, and J. Steinhoff, Quasinormal modes and their excitation beyond general relativity, *Phys. Rev. D* **110**, 024042 (2024), [arXiv:2404.11110 \[gr-qc\]](#).
- [18] P. A. Cano and A. Ruipérez, Leading higher-derivative corrections to Kerr geometry, *JHEP* **05**, 189, [Erratum: *JHEP* 03, 187 (2020)], [arXiv:1901.01315 \[gr-qc\]](#).
- [19] C. de Rham, J. Francfort, and J. Zhang, Black Hole Gravitational Waves in the Effective Field Theory of Gravity, *Phys. Rev. D* **102**, 024079 (2020), [arXiv:2005.13923 \[hep-th\]](#).
- [20] G. Goon, Heavy Fields and Gravity, *JHEP* **01**, 045, [Erratum: *JHEP* 03, 161 (2017)], [arXiv:1611.02705 \[hep-th\]](#).
- [21] S. Caron-Huot, Y.-Z. Li, J. Parra-Martinez, and D. Simmons-Duffin, Causality constraints on corrections to Einstein gravity, *JHEP* **05**, 122, [arXiv:2201.06602 \[hep-th\]](#).
- [22] G. T. Horowitz, M. Kolanowski, G. N. Remmen, and J. E. Santos, Extremal Kerr Black Holes as Amplifiers of New Physics, *Phys. Rev. Lett.* **131**, 091402 (2023), [arXiv:2303.07358 \[hep-th\]](#).
- [23] N. Sennett, R. Brito, A. Buonanno, V. Gorbenko, and L. Senatore, Gravitational-Wave Constraints on an Effective Field-Theory Extension of General Relativity, *Phys. Rev. D* **102**, 044056 (2020), [arXiv:1912.09917 \[gr-qc\]](#).
- [24] M. Accettulli Huber, A. Brandhuber, S. De Angelis, and G. Travaglini, From amplitudes to gravitational radiation with cubic interactions and tidal effects, *Phys. Rev. D* **103**, 045015 (2021), [arXiv:2012.06548 \[hep-th\]](#).
- [25] H. O. Silva, A. Ghosh, and A. Buonanno, Black-hole ringdown as a probe of higher-curvature gravity theories, *Phys. Rev. D* **107**, 044030 (2023), [arXiv:2205.05132 \[gr-qc\]](#).
- [26] P. A. Cano, B. Ganchev, D. R. Mayerson, and A. Ruipérez, Black hole multipoles in higher-derivative gravity, *JHEP* **12**, 120, [arXiv:2208.01044 \[gr-qc\]](#).
- [27] R. Cayuso, P. Figueras, T. França, and L. Lehner, Self-Consistent Modeling of Gravitational Theories beyond General Relativity, *Phys. Rev. Lett.* **131**, 111403 (2023).
- [28] A. Brandhuber, G. R. Brown, G. Travaglini, and P. Vives Matasan, Spinning quadrupoles in effective field theories of gravity (2024), [arXiv:2412.17958 \[hep-th\]](#).
- [29] S. Melville, Causality and quasi-normal modes in the GREFT, *Eur. Phys. J. Plus* **139**, 725 (2024), [arXiv:2401.05524 \[gr-qc\]](#).
- [30] S. Maenaut, G. Carullo, P. A. Cano, A. Liu, V. Cardoso, T. Hertog, and T. G. F. Li, Ringdown analysis of rotating black holes in effective field theory extensions of general relativity, *Phys. Rev. D* **113**, 044039 (2026), [arXiv:2411.17893 \[gr-qc\]](#).
- [31] P. Figueras, A. Held, and Á. D. Kovács, Well-posed initial value formulation of general effective field theories of gravity (2024), [arXiv:2407.08775 \[gr-qc\]](#).
- [32] L. Bernard, S. Giri, L. Lehner, and R. Sturani, Generic EFT-motivated beyond general relativity gravitational wave tests and their curvature dependence: From observation to interpretation, *Phys. Rev. D* **112**, 124013 (2025), [arXiv:2507.17143 \[gr-qc\]](#).
- [33] K. Martel and E. Poisson, Gravitational perturbations of the Schwarzschild spacetime: A Practical covariant and gauge-invariant formalism, *Phys. Rev. D* **71**, 104003 (2005), [arXiv:gr-qc/0502028](#).
- [34] P. A. Cano, K. Fransen, T. Hertog, and S. Maenaut, Gravitational ringing of rotating black holes in higher-derivative gravity, *Phys. Rev. D* **105**, 024064 (2022), [arXiv:2110.11378 \[gr-qc\]](#).
- [35] M. Lenzi and C. F. Sopuerta, Darboux covariance: A hidden symmetry of perturbed Schwarzschild black holes, *Phys. Rev. D* **104**, 124068 (2021), [arXiv:2109.00503 \[gr-qc\]](#).
- [36] M. Lenzi, A. M. Agudo, and C. F. Sopuerta, Korteweg-de Vries integrals for modified black hole potentials: instabilities and other questions, *JCAP* **09**, 021, [arXiv:2503.09918 \[gr-qc\]](#).
- [37] P. A. Cano, M. David, and G. van der Velde, Eikonal quasinormal modes of highly-spinning black holes in higher-curvature gravity: a window into extremality (2025), [arXiv:2509.08664 \[gr-qc\]](#).
- [38] L.-M. Cao, M.-F. Ji, L.-B. Wu, and Y.-S. Zhou, Pseudospectrum and time-domain analysis of the EFT corrected black holes, *Phys. Rev. D* **112**, 124022 (2025), [arXiv:2508.13894 \[gr-qc\]](#).
- [39] K. Nakashi, M. Kimura, H. Motohashi, and K. Takahashi, Probing higher curvature gravity via ringdown with overtones (2025), [arXiv:2512.22728 \[gr-qc\]](#).
- [40] C.-W. Shu and S. Osher, Efficient Implementation of Essentially Non-oscillatory Shock-Capturing Schemes, *Journal of Computational Physics* **77**, 439 (1988).
- [41] E. Chaverra, J. C. Degollado, C. Moreno, and O. Sarbach, Black holes in nonlinear electrodynamics: Quasinormal spectra and parity splitting, *Phys. Rev. D* **93**, 123013 (2016), [arXiv:1605.04003 \[gr-qc\]](#).
- [42] S. Chandrasekhar, On One-Dimensional Potential Barriers Having Equal Reflexion and Transmission Coefficients, *Proceedings of the Royal Society of London Series A* **369**, 425 (1980).

- [43] J. T. Gálvez Ghersi, A. V. Frolov, and D. A. Dobre, Echoes from the scattering of wavepackets on wormholes, *Class. Quant. Grav.* **36**, 135006 (2019), arXiv:1901.06625 [gr-qc].
- [44] C. T. Cunningham, R. H. Price, and V. Moncrief, Radiation from collapsing relativistic stars. I - Linearized odd-parity radiation, *Astrophys. J.* **224**, 643 (1978).
- [45] C. T. Cunningham, R. H. Price, and V. Moncrief, Radiation from collapsing relativistic stars. II. Linearized even parity radiation, *Astrophys. J.* **230**, 870 (1979).
- [46] J. R. Oppenheimer and H. Snyder, On Continued gravitational contraction, *Phys. Rev.* **56**, 455 (1939).
- [47] S. Trachanas, *Exactly solvable quantum mechanical potentials* (Crete University Press, 2009) [In Greek].
- [48] V. Baibhav, M. H.-Y. Cheung, E. Berti, V. Cardoso, G. Carullo, R. Cotesta, W. Del Pozzo, and F. Duque, Agnostic black hole spectroscopy: Quasinormal mode content of numerical relativity waveforms and limits of validity of linear perturbation theory, *Phys. Rev. D* **108**, 104020 (2023), arXiv:2302.03050 [gr-qc].
- [49] P. J. Nee, S. H. Völkel, and H. P. Pfeiffer, Role of black hole quasinormal mode overtones for ringdown analysis, *Phys. Rev. D* **108**, 044032 (2023), arXiv:2302.06634 [gr-qc].
- [50] S. Thomopoulos, S. H. Völkel, and H. P. Pfeiffer, Ringdown spectroscopy of phenomenologically modified black holes, *Phys. Rev. D* **112**, 064054 (2025), arXiv:2504.17848 [gr-qc].
- [51] P. Virtanen, R. Gommers, T. E. Oliphant, M. Haberland, T. Reddy, D. Cournapeau, E. Burovski, P. Peterson, W. Weckesser, J. Bright, S. J. van der Walt, M. Brett, J. Wilson, K. J. Millman, N. Mayorov, A. R. J. Nelson, E. Jones, R. Kern, E. Larson, C. J. Carey, Í. Polat, Y. Feng, E. W. Moore, J. VanderPlas, D. Laxalde, J. Perktold, R. Cimrman, I. Henriksen, E. A. Quintero, C. R. Harris, A. M. Archibald, A. H. Ribeiro, F. Pedregosa, P. van Mulbregt, and SciPy 1.0 Contributors, SciPy 1.0: Fundamental Algorithms for Scientific Computing in Python, *Nature Methods* **17**, 261 (2020).
- [52] M. Davis and R. Ruffini, Gravitational radiation in the presence of a Schwarzschild black hole. A boundary value search, *Lett. Nuovo Cim.* **2S2**, 1165 (1971).
- [53] M. Davis, R. Ruffini, W. H. Press, and R. H. Price, Gravitational radiation from a particle falling radially into a Schwarzschild black hole, *Phys. Rev. Lett.* **27**, 1466 (1971).
- [54] R. Ruffini, Gravitational radiation from a mass projected into a Schwarzschild black hole, *Phys. Rev. D* **7**, 972 (1973).
- [55] G. Tambalo, D. Watarai, H. O. Silva, K. Glampedakis, and K. Yagi (in preparation).
- [56] K. Glampedakis and N. Andersson, Late time dynamics of rapidly rotating black holes, *Phys. Rev. D* **64**, 104021 (2001), arXiv:gr-qc/0103054.
- [57] S. H. Völkel and A. Dhani, Quantifying systematic biases in black hole spectroscopy, *Phys. Rev. D* **112**, 084076 (2025), arXiv:2507.22122 [gr-qc].
- [58] P. A. Cano, K. Fransen, T. Hertog, and S. Maenaut, Quasinormal modes of rotating black holes in higher-derivative gravity, *Phys. Rev. D* **108**, 124032 (2023), arXiv:2307.07431 [gr-qc].
- [59] P. A. Cano, L. Capuano, N. Franchini, S. Maenaut, and S. H. Völkel, Parametrized quasinormal mode framework for modified Teukolsky equations, *Phys. Rev. D* **110**, 104007 (2024), arXiv:2407.15947 [gr-qc].
- [60] D. Brizuela, J. M. Martin-Garcia, and G. A. Mena Marugan, xPert: Computer algebra for metric perturbation theory, *Gen. Rel. Grav.* **41**, 2415 (2009), arXiv:0807.0824 [gr-qc].
- [61] J. M. Martin-Garcia, R. Portugal, and L. R. U. Manssur, The Invar Tensor Package, *Comput. Phys. Commun.* **177**, 640 (2007), arXiv:0704.1756 [cs.SC].
- [62] J. M. Martin-Garcia, D. Yllanes, and R. Portugal, The Invar tensor package: Differential invariants of Riemann, *Comput. Phys. Commun.* **179**, 586 (2008), arXiv:0802.1274 [cs.SC].
- [63] J. M. Martin-Garcia, xPerm: fast index canonicalization for tensor computer algebra, *Computer Physics Communications* **179**, 597 (2008), arXiv:0803.0862 [cs-sc].
- [64] *xAct: Efficient tensor computer algebra for the Wolfram Language*, <http://www.xact.es/>.
- [65] R. M. Corless, G. H. Gonnet, D. E. G. Hare, D. J. Jeffrey, and D. E. Knuth, On the Lambert  $W$  function, *Adv. Comput. Math.* **5**, 329 (1996).
- [66] P. Boonserm and M. Visser, Bounding the greybody factors for Schwarzschild black holes, *Phys. Rev. D* **78**, 101502 (2008), arXiv:0806.2209 [gr-qc].
- [67] Boost C++ Libraries, (<https://www.boost.org>).
- [68] M. Alcubierre, *Introduction to 3+1 Numerical Relativity* (2008).
- [69] V. Cardoso, M. Kimura, A. Maselli, E. Berti, C. F. B. Macedo, and R. McManus, Parametrized black hole quasinormal ringdown: Decoupled equations for non-rotating black holes, *Phys. Rev. D* **99**, 104077 (2019), arXiv:1901.01265 [gr-qc].
- [70] J. A. V. Kroon and L. J. G. Da Silva, The d'Alembert solution in hyperboloidal foliations, *Gen. Rel. Grav.* **56**, 85 (2024), arXiv:2403.07045 [gr-qc].